Spatio-angular fluorescence microscopy I. Basic theory (Draft: December 14, 2018)

TALON CHANDLER,[1,*] HARI SHROFF,[2,3] RUDOLF OLDENBOURG,[3] AND PATRICK LA RIVIÈRE[1,3]

[1] *University of Chicago, Department of Radiology, Chicago, Illinois 60637, USA*
[2] *Section on High Resolution Optical Imaging, National Institute of Biomedical Imaging and Bioengineering, National Institutes of Health, Bethesda, Maryland 20892, USA*
[3] *Marine Biological Laboratory, Bell Center, Woods Hole, Massachusetts 02543, USA*
[*] *talonchandler@talonchandler.com*

Abstract: We introduce the basic elements of a spatio-angular theory of fluorescence microscopy. We start by modeling an aplanatic microscope imaging an ensemble of in-focus fluorescent dipoles as a linear Hilbert-space operator, and we show that the operator takes a particularly convenient form when expressed in a basis of complex exponentials and spherical harmonics—a form we call the dipole spatio-angular transfer function. We demonstrate our formalism by analyzing a single-view fluorescence microscope without using the monopole or scalar approximations. We show that this imaging system has a spatio-angular band limit, and we exploit the band limit to perform efficient simulations. Notably, we show that information about the out-of-plane orientation of ensembles of in-focus fluorophores is recorded by paraxial fluorescence microscopes.

1. Introduction

Fluorescence microscopes are widely used in the biological sciences for measuring ensembles of fluorescent molecules that label specific proteins and biologically important molecules. While most fluorescence microscopy experiments are designed to measure only the spatial distribution of fluorophores, a growing number of experiments seek to measure both the spatial and angular distributions of fluorophores by the use of polarizers [1–5] or point spread function engineering [6, 7].

Meanwhile, single-molecule localization microscopy (SMLM) experiments use spatially sparse fluorescent samples to localize single molecules with precision that surpasses the diffraction limit. Noise limits the precision of this localization [8, 9], and several studies have shown that model mismatch (e.g. ignoring the effects of vector optics, dipole orientation [10], and dipole rotation [11]) can introduce localization bias as well. Therefore, the most precise and accurate SMLM experiments must use an appropriate model and jointly estimate both the position and orientation of each fluorophore. Several studies have successfully used vector optics and dipole models to estimate the position and orientation of single molecules [12–15], and there is growing interest in designing optical systems for measuring the position, orientation, and rotational dynamics of single molecules [6, 7, 16–18].

While many studies have focused on improving imaging models for spatially sparse fluorescent samples, we consider the more general case and aim to improve imaging models for arbitrary samples including those containing ensembles of fluorophores within a resolvable volume. In particular, we examine the effects of two widely used approximations in fluorescence microscopy—the *monopole approximation* and the *scalar approximation*.

We use the term *monopole* to refer to a model of a fluorophore that treats it as an isotropic absorber/emitter. Although the term *monopole approximation* is not in widespread use, we think it accurately describes the way many models of fluorescence microscopes treat fluorophores, and we use the term to distinguish the monopole model from more realistic dipole and higher-order models. Despite their use in models, electromagnetic monopole absorber/emitters do not exist in

nature. All physical fluorophores absorb and emit radiation with dipole or higher-order transitions, and these transitions are always oriented in space. For a classical mental model of fluorophores we imagine each dipole as a small oriented antenna (with incoherent absorption and emission moments) where electrons are constrained to move along a single direction. With this model we can argue classically that monopole radiators do not exist because they would violate the conservation of charge.

Although many works implicitly apply the monopole approximation, we have encountered two explicit justifications: (1) the sample contains many randomly oriented fluorophores within a resolvable volume or (2) the sample contains unconstrained rotating fluorophores. While both of these situations yield monopole-like samples, neither yields a sample that is perfectly described by the monopole model. In this work we investigate the dipole model of fluorophores in detail and find the conditions under which the monopole approximation is justified.

All fluorescence microscopy techniques that use an *optical point spread function* or an *optical transfer function* to model the mapping between the fluorophores and the irradiance on the detector implicitly make the monopole approximation. The optical point spread function is the irradiance response of an optical system to an isotropic point source, so it cannot model the response due to an anisotropic dipole radiator. In this work we define *monopole and dipole transfer functions* that describe the mapping between fluorophores and the measured irradiance. Although optical systems are an essential part of microscopes, fluorescence microscopists are interested in measuring the properties of fluorophores (not optics), so the monopole and dipole transfer functions are more directly useful than the optical transfer function for the problems that fluorescence microscopists are interested in solving.

While the monopole approximation applies to the fluorescent object, the *scalar approximation* applies to the fields that propagate through the microscope. Modeling the electric fields in a region requires a three-dimensional vector field, but if the electric fields are random or parallel a scalar field is sufficient, and we can replace the vector-valued electric field, $\mathbf{E}$, with a scalar-valued field, U.

The scalar approximation is often made together with the monopole approximation. For example, the Born-Wolf model [19] and the Gibson-Lanni model [20] make both the monopole and scalar approximations when applied to fluorescence microscopes. However, some models make the monopole approximation but not the scalar approximation. For example, the Richards-Wolf model [21] considers the role of vector-valued fields in the optical system, but it is an optical model so when it is applied to fluorescence microscopes the monopole approximation is assumed.

This work lies at the intersection of three fluorescence microscopy communities: (1) the spatial ensemble imaging community where many fluorophores are imaged in parallel and the goal is to find their concentration throughout the sample, (2) the spatio-angular ensemble community where many fluorophores are imaged in parallel and the goal is to find their concentration and orientation, and (3) the SMLM community where fluorophores are sparse in the sample and the goal is to find the position of each fluorophore. We briefly review how these three communities use the monopole and scalar approximations.

The large majority of fluorescence microscopes are used to image ensembles of fluorophores, and all existing restoration techniques make either or both of the monopole and scalar approximations. As discussed above, the Gibson-Lanni model, the Born-Wolf model, and the Richards-Wolf model are approximate when applied to fluorescence microscopes because they only model monopole emitters. Deconvolution algorithms that use these models may make biased estimates of fluorophore concentrations since they ignore the dipole excitation and emission of fluorophores, but we will see that these effects are small when the sample contains many randomly oriented fluorophores within a resolvable volume or unconstrained rotating fluorophores.

A small but growing group of microscopists is interested in measuring the orientation and position of ensembles of fluorophores [1–5]. These techniques typically use polarizers to make

multiple measurements of the same object, then they use a model of the dipole excitation and emission processes [22] to recover the orientation of fluorophores using pixel-wise arithmetic. Although these studies do not adopt the scalar or monopole approximations for the angular part of the problem, they adopt both approximations when they consider the spatial part of the problem. Existing works either ignore the spatial reconstruction problem [1–4] or assume that the spatial and angular reconstruction problems can be solved sequentially [5].

The most precise experiments in the SMLM community do not adopt the scalar or monopole approximations. Although many works have applied dipole models with vector optics, fewer have considered the effects of rotational or spatial diffusion, and to our knowledge no works have considered both rotational and spatial diffusion together. We will see that the dipole transfer functions are useful tools for incorporating angular and spatial diffusion into SMLM simulations and reconstructions.

In this work we place these three communities on a common theoretical footing. We begin in section 2 by formulating the imaging problem mathematically. We start with an abstract description of fluorescence imaging systems and extend the usual monopole imaging model to dipoles. Along the way we introduce transfer functions that will allow us to efficiently analyze spatio-angular microscopes. In section 3 we use the mathematical tools we developed in section 2 to analyze and simulate a single-view fluorescence microscope, and we demonstrate our techniques with four simple phantoms. Finally, in section 4 we discuss the results and their broader implications.

2. Theory

We begin our analysis with the abstract Hilbert space formalism of Barrett and Myers [23, ch. 1.3]. Our first task is to formulate the imaging process as a mapping between two Hilbert spaces $\mathcal{H} : \mathbb{U} \to \mathbb{V}$, where $\mathbb{U}$ is a set that contains all possible objects, $\mathbb{V}$ is a set that contains all (possibly noise-corrupted) datasets, and $\mathcal{H}$ is a model of the instrument that maps between these two spaces. We denote (possibly infinite-dimensional) Hilbert-space vectors in $\mathbb{U}$ with $\mathbf{f}$, Hilbert-space vectors in $\mathbb{V}$ with $\mathbf{g}$, and the mapping between the spaces with

$$\mathbf{g} = \mathcal{H}\mathbf{f}. \tag{1}$$

Throughout this work we will use the letters g, h, and f with varying fonts, capitalizations, and arguments to represent the data, the instrument, and the object, respectively.

Once we have identified the spaces $\mathbb{U}$ and $\mathbb{V}$, we can start expressing the mapping between the spaces in a specific object-space and data-space basis. In most cases the easiest mapping to find uses a delta-function basis—we expand object and data space into delta functions, then express the mapping as an integral transform. After finding this mapping we can start to investigate the same mapping in different bases.

The above discussion is quite abstract, but it is a powerful point of view that will enable us to unify the analysis of spatio-angular fluorescence microscopes. In section 2.1 we will demonstrate the formalism by examining a familiar monopole imaging model, and we will demonstrate the mapping between object and data space in two different bases. In section 2.2 we will extend the monopole imaging model to dipoles and examine the mapping in four different bases.

2.1. Monopole imaging in different bases

We start by considering a microscope that images a field of in-focus monopoles by recording the irradiance on a two-dimensional detector. This section treads familiar ground, but it serves to establish the concepts and notation that will be necessary when we extend to the dipole case.

We can represent the object as a function that assigns a real number to each point on a plane, so we identify object space as $\mathbb{U} = \mathbb{L}_2(\mathbb{R}^2)$—the set of square-integrable functions on

the two-dimensional plane. Similarly, we have a two-dimensional detector that measures a real number at each point on a plane, so data space is the same set $\mathbb{V} = \mathbb{L}_2(\mathbb{R}^2)$.

Next, we name the representations of our object and data in a specific basis. In a delta function basis the object can be represented by a function $f(\mathbf{r}_o)$ called the *monopole density*—the number of monopoles per unit area at the two-dimensional position $\mathbf{r}_o$. Similarly, in a delta function basis the data can be represented by a function $g'(\mathbf{r}_d')$ called the *irradiance*—the power received by a surface per unit area at position $\mathbf{r}_d'$. Note that we have adopted a slightly unusual convention of using primes to denote unscaled coordinates. Later in this section we will introduce unprimed scaled coordinates that we will use throughout the rest of the paper.

A reasonable starting point is to assume that the relationship between the object and the data is *linear*—this is true in many fluorescence microscopes because fluorophores emit incoherently, so a scaled sum of fluorophores will result in a scaled sum of the irradiance patterns created by the individual fluorophores. Note that our assumption of linearity excludes cases where fluorophores interact (e.g. homoFRET) or saturate (e.g. non-linear fluorescence microscopy).

If the mapping is linear, we can write the irradiance as a weighted integral over a field of monopoles

$$g'(\mathbf{r}_d') = \int_{\mathbb{R}^2} d\mathbf{r}_o \, h'(\mathbf{r}_d', \mathbf{r}_o) f(\mathbf{r}_o), \tag{2}$$

where $h'(\mathbf{r}_d', \mathbf{r}_o)$ is the irradiance at position $\mathbf{r}_d'$ created by a point source at $\mathbf{r}_o$.

Next, we assume that the optical system is *aplanatic*—Abbe's sine condition is satisfied and on-axis points are imaged without aberration. Abbe's sine condition guarantees that off-axis points are imaged without spherical aberration or coma [24, ch. 1], so the imaging system can be modeled within the field of view of the optical system as a magnifier with shift-invariant blur

$$g'(\mathbf{r}_d') = \int_{\mathbb{R}^2} d\mathbf{r}_o \, h'(\mathbf{r}_d' - m\mathbf{r}_o) f(\mathbf{r}_o), \tag{3}$$

where m is a magnification factor.

We can simplify our analysis by changing coordinates and writing Eq. (3) as a convolution [23, ch. 7.2.7]. We define a demagnified detector coordinate $\mathbf{r}_d = \mathbf{r}_d'/m$ and a normalization factor that corresponds to the total power incident on the detector plane due to a point source $P_{\text{mono}} = \int_{\mathbb{R}^2} d\mathbf{r} \, h'(m\mathbf{r})$ where $\mathbf{r} = \mathbf{r}_d - \mathbf{r}_o$. We use these scaling factors to define the *monopole point spread function* as

$$h(\mathbf{r}_d - \mathbf{r}_o) = \frac{h'(m[\mathbf{r}_d - \mathbf{r}_o])}{P_{\text{mono}}}, \tag{4}$$

and the *scaled irradiance* as

$$g(\mathbf{r}_d) = \frac{g'(m\mathbf{r}_d)}{P_{\text{mono}}}. \tag{5}$$

With these definitions we can express the mapping between the object and the data as a familiar convolution

$$g(\mathbf{r}_d) = \int_{\mathbb{R}^2} d\mathbf{r}_o \, h(\mathbf{r}_d - \mathbf{r}_o) f(\mathbf{r}_o). \tag{6}$$

We have chosen to normalize the monopole point spread function so that

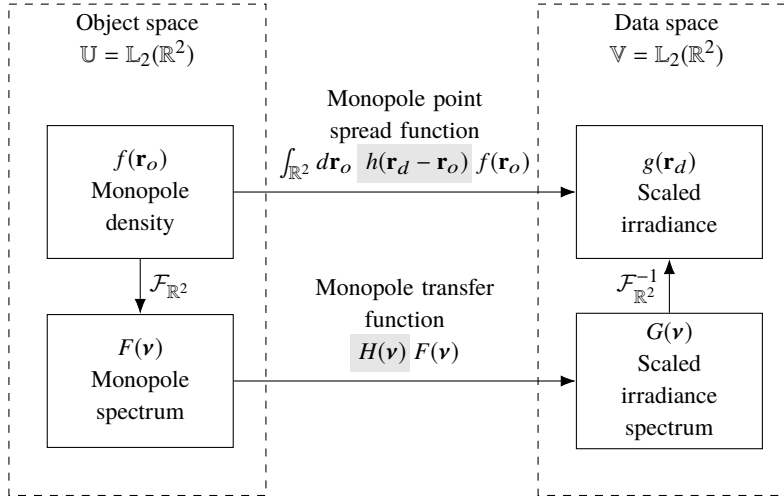$$\int_{\mathbb{R}^2} d\mathbf{r} \, h(\mathbf{r}) = 1. \tag{7}$$

Fig. 1. The mapping between the object and data space of a monopole fluorescence microscope can be computed in two different bases—a delta function basis and a complex exponential basis. The change of basis can be computed with a two-dimensional Fourier transform denoted $\mathcal{F}_{\mathbb{R}^2}$.

The monopole point spread function corresponds to a measurable irradiance, so it is always real and positive.

The mapping between the object and the data in a linear shift-invariant imaging system takes a particularly simple form in a complex exponential (i.e. Fourier) basis. If we apply the Fourier convolution theorem to Eq. (6) we find that

$$G(\boldsymbol{\nu}) = H(\boldsymbol{\nu})F(\boldsymbol{\nu}), \tag{8}$$

where we define the *scaled irradiance spectrum* as

$$G(\boldsymbol{\nu}) = \int_{\mathbb{R}^2} d\mathbf{r}\, g(\mathbf{r}) \exp(-2\pi i \mathbf{r} \cdot \boldsymbol{\nu}), \tag{9}$$

the *monopole transfer function* as

$$H(\boldsymbol{\nu}) = \int_{\mathbb{R}^2} d\mathbf{r}\, h(\mathbf{r}) \exp(-2\pi i \mathbf{r} \cdot \boldsymbol{\nu}), \tag{10}$$

and the *monopole spectrum* as

$$F(\boldsymbol{\nu}) = \int_{\mathbb{R}^2} d\mathbf{r}\, f(\mathbf{r}) \exp(-2\pi i \mathbf{r} \cdot \boldsymbol{\nu}). \tag{11}$$

The monopole point spread function is normalized and real, so we know that the monopole transfer function is normalized, $H(0) = 1$, and conjugate symmetric, $H(-\boldsymbol{\nu}) = H^*(\boldsymbol{\nu})$, where z^* denotes the complex conjugate of z.

Notice that Eqs. (6) and (8) are expressions of the same mapping between object and data space in different bases. Figure 1 summarizes the relationship between object and data space in both bases.

We have been careful to use the term *monopole transfer function* instead of the commonly-used term *optical transfer function*. We reserve the term *optical transfer function* for optical systems— the optical transfer function maps between an input irradiance spectrum and an output irradiance

spectrum in an optical system. We can use optical transfer functions to model the propagation of light through a microscope, but ultimately we are always interested in the object, not the light emitted by the object. We will find the distinction between the optical transfer function and the object transfer function to be especially valuable when we consider dipoles later in this section.

2.1.1. Monopole coherent transfer functions

Although the Fourier transform can be used to calculate the monopole transfer function directly from the monopole point spread function, there is a well-known alternative that exploits coherent transfer functions. The key idea is that the monopole point spread function can always be written as the absolute square of a scalar-valued *monopole coherent spread function*, $c(\mathbf{r}_d - \mathbf{r}_o)$, defined by

$$|c(\mathbf{r}_d - \mathbf{r}_o)|^2 = h(\mathbf{r}_d - \mathbf{r}_o). \tag{12}$$

Physically, the monopole coherent spread function corresponds to the scalar-valued field on the detector with appropriate scaling.

We can plug Eq. (12) into Eq. (10) and use the autocorrelation theorem to rewrite the monopole transfer function as

$$H(\boldsymbol{\nu}) = \int_{\mathbb{R}^2} d\boldsymbol{\tau} \, C(\boldsymbol{\tau}) C^*(\boldsymbol{\tau} - \boldsymbol{\nu}), \tag{13}$$

where we have introduced the *monopole coherent transfer function* as the two-dimensional Fourier transform of the monopole coherent spread function:

$$C(\boldsymbol{\tau}) = \int_{\mathbb{R}^2} d\mathbf{r} \, c(\mathbf{r}) \exp[-2\pi i \mathbf{r} \cdot \boldsymbol{\tau}]. \tag{14}$$

Physically, the monopole coherent transfer function corresponds to the scalar-valued field in a Fourier plane of the detector with appropriate scaling.

The coherent transfer function provides a valuable shortcut for analyzing microscopes since it is often straightforward to calculate the field in a Fourier plane of the detector. A typical approach for calculating the transfer functions is to (1) calculate the field in a Fourier plane of the detector, (2) scale the field to find the monopole coherent transfer function, then (3) use the relationships in Fig. 2 to calculate the other transfer functions.

2.2. Dipole imaging in different bases

Now we consider a microscope imaging a field of in-focus dipoles by recording the irradiance on a two-dimensional detector. A function that assigns a real number to each point on a plane is not sufficient to specify a field of dipoles because the dipoles can have different orientations. To represent the object we need to extend object space to $\mathbb{U} = \mathbb{L}_2(\mathbb{R}^2 \times \mathbb{S}^2)$—the set of square-integrable functions on the product space of a plane and a two-dimensional sphere (the usual sphere embedded in $\mathbb{R}^3$). To visualize functions in object space we imagine a sphere at every point on a plane with a scalar value assigned to every point on each sphere.

In a delta function basis the object can be represented by a function $f(\mathbf{r}_o, \hat{\mathbf{s}}_o)$ called the *dipole density*—the number of dipoles per unit area and per unit solid angle at position $\mathbf{r}_o$ and oriented along $\hat{\mathbf{s}}_o$. Similar to the monopole case, we model the mapping between the object and the irradiance in a delta function basis as an integral transform

$$g'(\mathbf{r}'_d) = \int_{\mathbb{S}^2} d\hat{\mathbf{s}}_o \int_{\mathbb{R}^2} d\mathbf{r}_o \, h'(\mathbf{r}'_d, \mathbf{r}_o, \hat{\mathbf{s}}_o) f(\mathbf{r}_o, \hat{\mathbf{s}}_o), \tag{15}$$
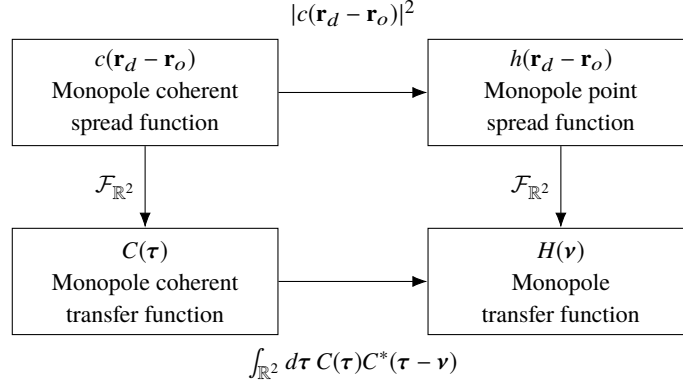
Fig. 2. The monopole transfer functions are related by a two-dimensional Fourier transform (right column). The coherent monopole transfer functions (left column) can be used to simplify the calculation of the remaining transfer functions.

where $h'(\mathbf{r}'_d, \mathbf{r}_o, \hat{\mathbf{s}}_o)$ is the irradiance at position $\mathbf{r}'_d$ created by a point source at $\mathbf{r}_o$ with orientation $\hat{\mathbf{s}}_o$. Notice that we have considered all possible orientations $\hat{\mathbf{s}}_o$ and integrated over the sphere $\mathbb{S}^2$. The dipole density is always symmetric under angular inversion, $f(\mathbf{r}_o, \hat{\mathbf{s}}_o) = f(\mathbf{r}_o, -\hat{\mathbf{s}}_o)$, so we could have chosen to integrate over a hemisphere and adjusted the definition the dipole density by a factor of two. For convenience we will continue to integrate over the complete sphere. We note that all functions in this work with $\hat{\mathbf{s}}_o$ as an independent variable are symmetric under angular inversion, $\hat{\mathbf{s}}_o \rightarrow -\hat{\mathbf{s}}_o$.

If the optical system is aplanatic, we can write the integral transform as

$$g'(\mathbf{r}'_d) = \int_{\mathbb{S}^2} d\hat{\mathbf{s}}_o \int_{\mathbb{R}^2} d\mathbf{r}_o \, h'(\mathbf{r}'_d - m\mathbf{r}_o, \hat{\mathbf{s}}_o) f(\mathbf{r}_o, \hat{\mathbf{s}}_o). \tag{16}$$

We define the same demagnified detector coordinate $\mathbf{r}_d = \mathbf{r}'_d/m$ and a new normalization factor that corresponds to the total power incident on the detector due to a spatial point source with an angularly uniform distribution of dipoles $P_{\text{dip}} = \int_{\mathbb{S}^2} d\hat{\mathbf{s}}_o \int_{\mathbb{R}^2} d\mathbf{r} \, h'(m\mathbf{r}, \hat{\mathbf{s}}_o)$. We use these scaling factors to define the *dipole point spread function* as

$$h(\mathbf{r}_d - \mathbf{r}_o, \hat{\mathbf{s}}_o) = \frac{h'(m[\mathbf{r}_d - \mathbf{r}_o], \hat{\mathbf{s}}_o)}{P_{\text{dip}}}, \tag{17}$$

and the *scaled irradiance* as

$$g(\mathbf{r}_d) = \frac{g'(m\mathbf{r}_d)}{P_{\text{dip}}}. \tag{18}$$

With these definitions we can express the mapping between the object and the data as

$$g(\mathbf{r}_d) = \int_{\mathbb{S}^2} d\hat{\mathbf{s}}_o \int_{\mathbb{R}^2} d\mathbf{r}_o \, h(\mathbf{r}_d - \mathbf{r}_o, \hat{\mathbf{s}}_o) f(\mathbf{r}_o, \hat{\mathbf{s}}_o). \tag{19}$$

Equation (19) is a key result because it represents the mapping between object space and data space in a delta function basis. The integrals in Eq. (19) would be extremely expensive to compute for an arbitrary object, but the integrals simplify to an efficient sum if the object is spatially and angularly sparse. In other words, Eq. (19) is ideal for simulating and analyzing single fluorophores that are rigidly attached to an oriented structure.

Similar to the monopole case, we have chosen to normalize the dipole point spread function so that

$$\int_{\mathbb{S}^2} d\hat{\mathbf{s}}_o \int_{\mathbb{R}^2} d\mathbf{r}\, h(\mathbf{r}, \hat{\mathbf{s}}_o) = 1. \tag{20}$$

The dipole point spread function is a measurable quantity, so it is real and positive.

2.2.1. Dipole spatial transfer function

We can make our first change of basis by applying the Fourier-convolution theorem to Eq. (19), which yields

$$G(\boldsymbol{\nu}) = \int_{\mathbb{S}^2} d\hat{\mathbf{s}}_o\, H(\boldsymbol{\nu}, \hat{\mathbf{s}}_o) F(\boldsymbol{\nu}, \hat{\mathbf{s}}_o), \tag{21}$$

where we define the *dipole spatial transfer function* as

$$H(\boldsymbol{\nu}, \hat{\mathbf{s}}_o) = \int_{\mathbb{R}^2} d\mathbf{r}\, h(\mathbf{r}, \hat{\mathbf{s}}_o) \exp(-2\pi i \mathbf{r} \cdot \boldsymbol{\nu}), \tag{22}$$

and the *dipole spatial spectrum* as

$$F(\boldsymbol{\nu}, \hat{\mathbf{s}}_o) = \int_{\mathbb{R}^2} d\mathbf{r}\, f(\mathbf{r}, \hat{\mathbf{s}}_o) \exp(-2\pi i \mathbf{r} \cdot \boldsymbol{\nu}). \tag{23}$$

Since the dipole point spread function is normalized and real, we know that the dipole spatial transfer function is normalized, $\int_{\mathbb{S}^2} d\hat{\mathbf{s}}\, H(0, \hat{\mathbf{s}}_o) = 1$, and conjugate symmetric, $H(-\boldsymbol{\nu}, \hat{\mathbf{s}}_o) = H^*(\boldsymbol{\nu}, \hat{\mathbf{s}}_o)$.

This basis is ideal for simulating and analyzing objects that are angularly sparse and spatially dense; e.g. rod-like structures that contain fluorophores in a fixed orientation, or rotationally fixed fluorophores that are undergoing spatial diffusion.

2.2.2. Dipole angular transfer function

The spherical harmonics are another set of convenient basis functions that play the same role as complex exponentials in spatial transfer functions—see Appendix A for an introduction to the spherical harmonics. We can change basis from spherical delta functions to spherical harmonics by applying the generalized Plancherel theorem for spherical functions

$$\int_{\mathbb{S}^2} d\hat{\mathbf{s}}\, p(\hat{\mathbf{s}}) q^*(\hat{\mathbf{s}}) = \sum_{\ell=0}^{\infty} \sum_{m=-\ell}^{\ell} P_\ell^m Q_\ell^{m*}, \tag{24}$$

where $p(\hat{\mathbf{s}})$ and $q(\hat{\mathbf{s}})$ are arbitrary functions on the sphere, P_ℓ^m and Q_ℓ^m are their spherical Fourier transforms defined by

$$P_\ell^m = \int_{\mathbb{S}^2} d\hat{\mathbf{s}}\, p(\hat{\mathbf{s}}) Y_\ell^{m*}(\hat{\mathbf{s}}), \tag{25}$$

and $Y_\ell^m(\hat{\mathbf{s}})$ are the spherical harmonic functions defined in Appendix A. Equation (24) expresses the fact that scalar products are invariant under a change of basis [23, Eq. 3.78]. The left-hand side of Eq. (24) is the scalar product of $\mathbb{L}_2(\mathbb{S}^2)$ functions in a delta function basis and the right-hand side is the scalar product of $\mathbb{L}_2(\mathbb{S}^2)$ functions in a spherical harmonic function basis. Applying Eq. (24) to Eq. (19) yields

$$g(\mathbf{r}_d) = \sum_{\ell=0}^{\infty} \sum_{m=-\ell}^{\ell} \int_{\mathbb{R}^2} d\mathbf{r}_o\, H_\ell^m(\mathbf{r}_d - \mathbf{r}_o) F_\ell^m(\mathbf{r}_o), \tag{26}$$
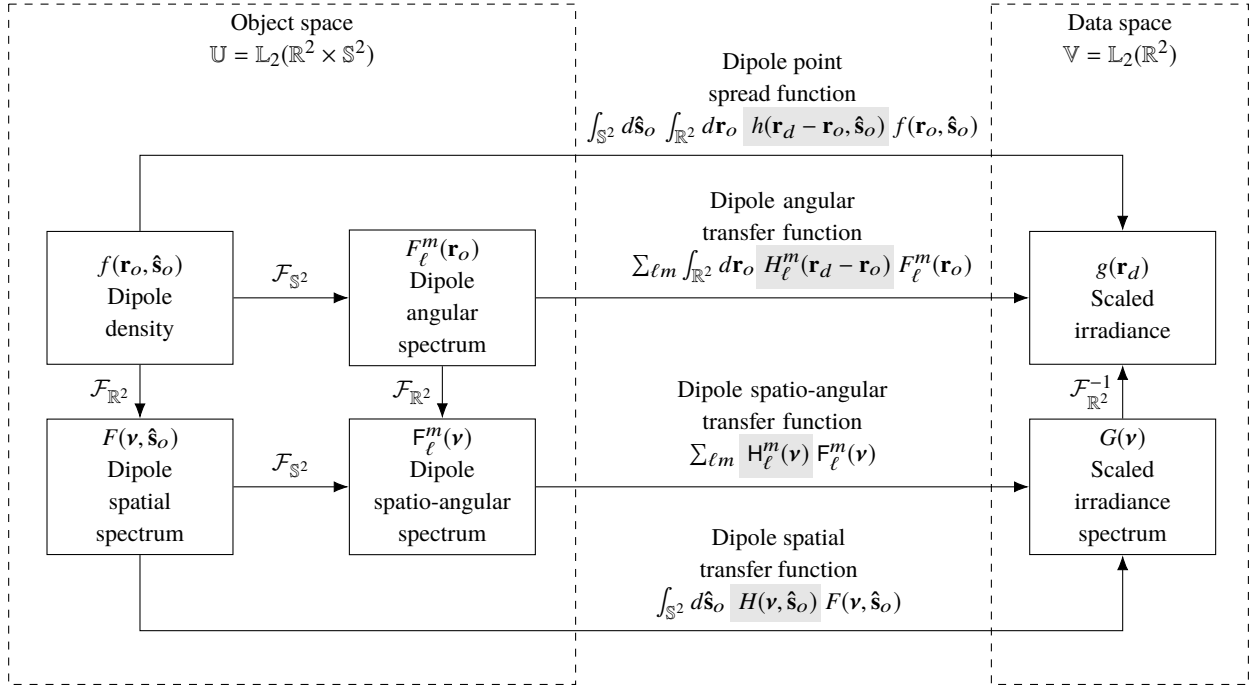
Fig. 3. The mapping between the object space and data space of a dipole imaging system can be computed in four different bases—a delta function basis, a complex-exponential/angular-delta basis, a spatial-delta/spherical-harmonic basis, and a complex-exponential/spherical-harmonic basis. The changes of basis can be computed with the two-dimensional Fourier transform denoted $\mathcal{F}_{\mathbb{R}^2}$, and the spherical Fourier transform denoted $\mathcal{F}_{\mathbb{S}^2}$.

where we have defined the *dipole angular transfer function* as

$$H_\ell^m(\mathbf{r}_d - \mathbf{r}_o) = \int_{\mathbb{S}^2} d\hat{\mathbf{s}}_o \, h(\mathbf{r}_d - \mathbf{r}_o, \hat{\mathbf{s}}_o) Y_\ell^{m*}(\hat{\mathbf{s}}_o), \tag{27}$$

and the *dipole angular spectrum* as

$$F_\ell^m(\mathbf{r}_o) = \int_{\mathbb{S}^2} d\hat{\mathbf{s}}_o \, f(\mathbf{r}_o, \hat{\mathbf{s}}_o) Y_\ell^{m*}(\hat{\mathbf{s}}_o). \tag{28}$$

Since the dipole point spread function is normalized and real, we know that the dipole angular transfer function is normalized, $\int_{\mathbb{R}^2} d\mathbf{r} \, H_0^0(\mathbf{r}) = 1$, and conjugate symmetric, $H_\ell^{-m}(\mathbf{r}) = (-1)^m H_\ell^{m*}(\mathbf{r})$.

This basis is well suited for simulating and analyzing objects that are spatially sparse and angularly dense; e.g. single fluorophores that are undergoing angular diffusion, or many fluorophores that are within a resolvable volume with varying orientations.

2.2.3. Spatio-angular dipole transfer function

We can arrive at our final basis in two ways: by applying the generalized Plancherel theorem for spherical functions to Eq. (21) or by applying the Fourier convolution theorem to Eq. (26). We follow the first path and find that

$$G(\boldsymbol{\nu}) = \sum_{\ell=0}^\infty \sum_{m=-\ell}^\ell \mathsf{H}_\ell^m(\boldsymbol{\nu}) \mathsf{F}_\ell^m(\boldsymbol{\nu}), \tag{29}$$
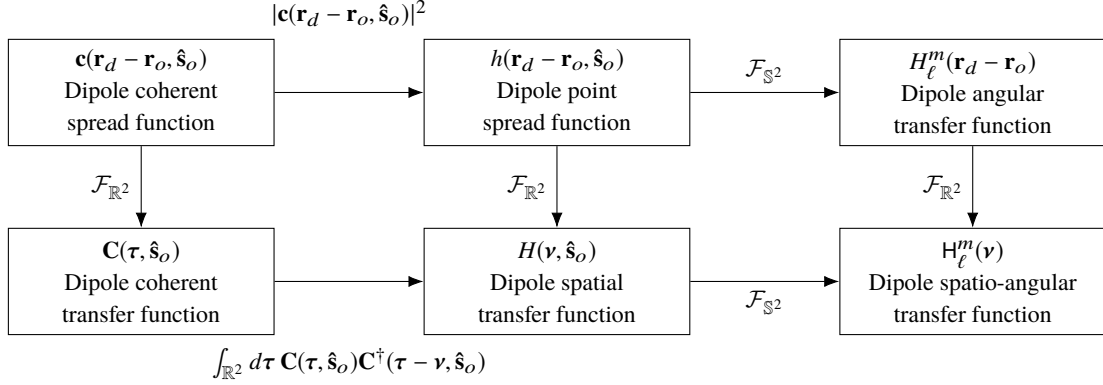
Fig. 4. There is one transfer function for each set of object-space basis functions, and these transfer functions are related by two-dimensional and spherical Fourier transforms—see center and right columns. There is an additional pair of coherent transfer functions that are useful for calculating the transfer functions—see left column.

where we have defined the *dipole spatio-angular transfer function* as

$$\mathsf{H}_\ell^m(\nu) = \int_{\mathbb{S}^2} d\hat{\mathbf{s}}_o \, H(\nu, \hat{\mathbf{s}}_o) Y_\ell^{m*}(\hat{\mathbf{s}}_o), \tag{30}$$

and the *dipole spatio-angular spectrum* as

$$\mathsf{F}_\ell^m(\nu) = \int_{\mathbb{S}^2} d\hat{\mathbf{s}}_o \, F(\nu, \hat{\mathbf{s}}_o) Y_\ell^{m*}(\hat{\mathbf{s}}_o). \tag{31}$$

Since the dipole point spread function is normalized and real, we know that the dipole spatio-angular transfer function is normalized, $\mathsf{H}_0^0(0) = 1$, and conjugate symmetric, $\mathsf{H}_\ell^{-m}(-\nu) = (-1)^m \mathsf{H}_\ell^{m*}(\nu)$.

This basis is well suited for simulating and analyzing arbitrary samples because it exploits the band limit of the imaging system. We will see the advantage explicitly in Section 3 when we calculate a specific dipole spatio-angular transfer function and see that it has spatial and angular band limits. We note that most single molecule imaging experiments are best described in this basis because of the effects of spatial and rotational diffusion.

Figure 3 summarizes the relationships between the four bases that we can use to compute the image of a field of dipoles. We reiterate that all four bases may be useful depending on the sample.

2.2.4. Dipole coherent transfer functions

Similar to the monopole case, there is an efficient way to calculate the transfer functions using coherent transfer functions. The dipole point spread function can always be written as the absolute square of a vector-valued function, $\mathbf{c}(\mathbf{r}_d - \mathbf{r}_o, \hat{\mathbf{s}}_o)$, called the *dipole coherent spread function*:

$$|\mathbf{c}(\mathbf{r}_d - \mathbf{r}_o, \hat{\mathbf{s}}_o)|^2 = h(\mathbf{r}_d - \mathbf{r}_o, \hat{\mathbf{s}}_o). \tag{32}$$

Physically, the dipole coherent spread function corresponds to the vector-valued electric field on the detector with appropriate scaling. We need a vector-valued coherent transfer function since the polarization of the field plays a significant role in dipole imaging, so the dipole point spread function cannot be written as an absolute square of a scalar-valued function.

We can plug Eq. (32) into Eq. (22) and use the autocorrelation theorem to rewrite the dipole spatial transfer function as

$$H(\boldsymbol{\nu}, \hat{\mathbf{s}}_o) = \int_{\mathbb{R}^2} d\boldsymbol{\tau} \, \mathbf{C}(\boldsymbol{\tau}, \hat{\mathbf{s}}_o) \mathbf{C}^\dagger(\boldsymbol{\tau} - \boldsymbol{\nu}, \hat{\mathbf{s}}_o), \tag{33}$$

where we have introduced the *dipole coherent transfer function* $\mathbf{C}(\boldsymbol{\tau}, \hat{\mathbf{s}}_o)$ as the two-dimensional Fourier transform of the dipole coherent spread function:

$$\mathbf{C}(\boldsymbol{\tau}, \hat{\mathbf{s}}_o) = \int_{\mathbb{R}^2} d\mathbf{r} \, \mathbf{c}(\mathbf{r}, \hat{\mathbf{s}}_o) \exp[-2\pi i \mathbf{r} \cdot \boldsymbol{\tau}]. \tag{34}$$

Physically, the dipole coherent transfer function corresponds to the vector-valued electric field created by a dipole oriented along $\hat{\mathbf{s}}_o$ in a Fourier plane of the detector with appropriate scaling. Similar to the monopole case, we can calculate the dipole-orientation-dependent fields in a Fourier plane of the detector, scale appropriately to find the dipole coherent transfer function, then use the relationships in Fig. 4 to calculate the other transfer functions. Finally, we note that the dipole coherent transfer function is identical to what Agrawal et. al. call the *Green's tensor* [6] and Novotny and Hecht's *dyadic point spread function* multiplied by the dipole moment vector [25].

3. Results

In this section we begin to apply the tools we developed in the previous section to analyze a specific fluorescence microscope. During our initial discussion we only required the optical system to be aplanatic so that we could model it as a shift-invariant magnifier. Now we will be more specific and consider an aplanatic optical system in a *4f configuration* with an arbitrary first lens (the objective lens) and a *paraxial second lens* (the tube lens) as shown in Fig. 5. A lens can be considered paraxial if the angle α between the optical axis of the lens and the marginal ray is small enough that $\sin\alpha \approx \alpha$. As a rule of thumb, non-paraxial effects only become significant when the numerical aperture of a lens exceeds 0.7 [26, ch. 6], but this is only a rough guideline. Commercial microscopes with infinity-corrected objectives can almost always can be modeled by considering the tube lens as paraxial.

We start by defining *pupil functions* for both monopole and dipole imaging systems, and we explicitly relate the pupil functions to the previously defined coherent transfer functions. After establishing the link between physical calculations and the transfer functions, we calculate the monopole and dipole transfer functions for imaging systems with a paraxial objective, and we demonstrate our approach by simulating simple phantoms.

3.1. Monopole pupil functions

We define the *monopole pupil function* $p(\mathbf{r}_p)$ of the imaging system as the field immediately following the pupil plane created by an on-axis monopole, where $\mathbf{r}_p$ is an unscaled two-dimensional coordinate in the pupil plane. In this section we will relate the monopole pupil function to the transfer function we defined in section 2 by adapting the treatment in Barrett and Myers [23, ch. 9.7].

Since monopoles emit scalar fields, the monopole pupil function is a scalar-valued function. The optical system is aplanatic, so we can write the field, $U_p(\mathbf{r}_p, \mathbf{r}_o)$, created at a point in the pupil plane $\mathbf{r}_p$ by a monopole at position $\mathbf{r}_o$ as

$$U_p(\mathbf{r}_p, \mathbf{r}_o) \propto p(\mathbf{r}_p) \exp\left[-2\pi i \frac{n_0}{\lambda f_0} \mathbf{r}_p \cdot \mathbf{r}_o\right]. \tag{35}$$
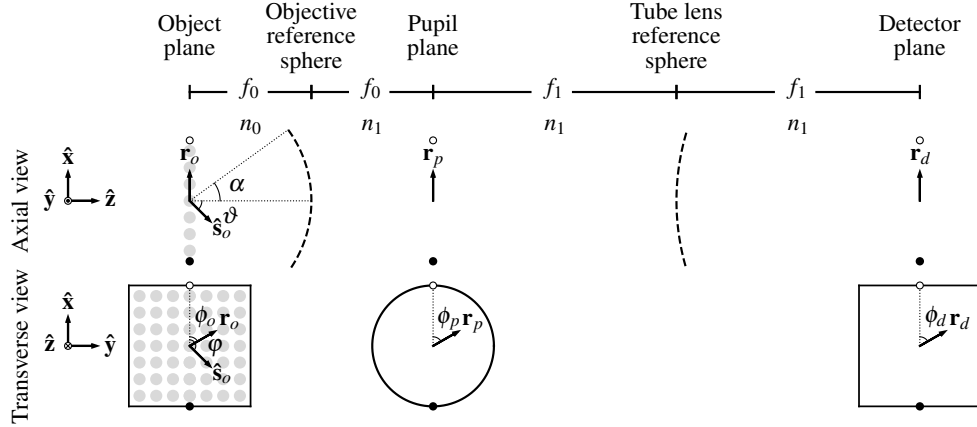
Fig. 5. Schematic of an aplanatic imaging system in a $4f$ geometry with a paraxial tube lens. We are considering an aplanatic optical system, so we only need to consider the image created by on-axis objects. The fluorescent object consists of ensembles of dipoles embedded in a medium with index of refraction n_0. An objective with focal length f_0 and numerical aperture NA $= n_o \sin \alpha$ is trained on the object. A paraxial tube lens with focal length f_1 and a detector complete the $4f$ geometry, and all components except the object are embedded in a medium with index of refraction n_1. The object, pupil, and detector planes are parameterized by vectors $\mathbf{r}_o$, $\mathbf{r}_p$, and $\mathbf{r}_d$ with polar coordinates (r_o, ϕ_o), (r_b, ϕ_b), and (r_d, ϕ_d), respectively. At each position $\mathbf{r}_o$ in the object there is a sphere parameterized by a unit vector $\hat{\mathbf{s}}_o$ with spherical coordinates (ϑ, φ).

Equation (35) is a restatement of the aplanatic condition for a $4f$ optical system—the fields in the pupil plane can be written as the pupil function multiplied by a linear phase factor that encodes the position of the object.

Since the second lens is paraxial, we can model the relationship between the field in the pupil plane and the field on the detector with a scaled Fourier transform [16, 27, 28]:

$$U_d(\mathbf{r}'_d, \mathbf{r}_o) \propto \int_{\mathbb{R}^2} d\mathbf{r}_p \, p(\mathbf{r}_p) \exp\left[-2\pi i \frac{n_0}{\lambda f_0} \mathbf{r}_p \cdot \mathbf{r}_o\right] \exp\left[-2\pi i \frac{n_1}{\lambda f_1} \mathbf{r}_p \cdot \mathbf{r}'_d\right]. \tag{36}$$

If we define $P(\boldsymbol{\tau})$ as the two-dimensional Fourier transform of the pupil function then we can rewrite Eq. (36) as

$$U_d(\mathbf{r}'_d, \mathbf{r}_o) \propto P\left(\frac{n_0}{\lambda f_0} \mathbf{r}_o + \frac{n_1}{\lambda f_1} \mathbf{r}'_d\right), \tag{37}$$

which we can simplify further by writing in terms of $m = -\frac{f_1 n_0}{f_0 n_1}$:

$$U_d(\mathbf{r}'_d - m\mathbf{r}_o) \propto P\left(\frac{n_1}{\lambda f_1} [\mathbf{r}'_d - m\mathbf{r}_o]\right). \tag{38}$$

The irradiance on the detector is the absolute square of the field so

$$h'(\mathbf{r}'_d - m\mathbf{r}_o) \propto \left| P\left(\frac{n_1}{\lambda f_1} [\mathbf{r}'_d - m\mathbf{r}_o]\right) \right|^2. \tag{39}$$

If we demagnify the coordinates with $\mathbf{r}_d = \mathbf{r}'_d/m$ and demagnify the irradiance with $h(\mathbf{r}_d - \mathbf{r}_o) \propto h'(m[\mathbf{r}_d - \mathbf{r}_o])$, we find that the monopole point spread function is related to the Fourier transform

of the monopole pupil function by

$$h(\mathbf{r}_d - \mathbf{r}_o) \propto \left| P\left(-\frac{n_o}{\lambda f_o}[\mathbf{r}_d - \mathbf{r}_o]\right)\right|^2. \tag{40}$$

The monopole point spread function is the absolute square of the monopole coherent spread function so

$$c(\mathbf{r}_d - \mathbf{r}_o) \propto P\left(-\frac{n_o}{\lambda f_o}[\mathbf{r}_d - \mathbf{r}_o]\right). \tag{41}$$

Finally, the monopole coherent transfer function is the Fourier transform of the monopole coherent spread function so

$$C(\boldsymbol{\tau}) \propto p\left(\frac{\lambda f_o}{n_o}\boldsymbol{\tau}\right). \tag{42}$$

Equation (42) is the key result of this section—the monopole coherent transfer function is a scaled monopole pupil function.

3.2. Dipole pupil function

We define the *dipole pupil function* $\mathbf{p}(\mathbf{r}_p, \hat{\mathbf{s}}_o)$ of the imaging system as the electric field immediately following the pupil plane created by an on-axis dipole oriented along $\hat{\mathbf{s}}_o$. Since dipoles emit vector-valued electric fields, the dipole pupil function is a vector-valued function. Almost all of the arguments in the previous section carry over to the dipole case. Briefly, we can write the electric field created at a point in the pupil $\mathbf{r}_p$ by a dipole at $\mathbf{r}_o$ oriented along $\hat{\mathbf{s}}_o$ as

$$\mathbf{E}(\mathbf{r}_p, \mathbf{r}_o, \hat{\mathbf{s}}_o) \propto \mathbf{p}(\mathbf{r}_p, \hat{\mathbf{s}}_o)\exp\left[-2\pi i \frac{n_0}{\lambda f_0}\mathbf{r}_p \cdot \mathbf{r}_o\right]. \tag{43}$$

The second lens is paraxial, so we can find the field on the detector with a Fourier transform

$$\mathbf{E}_d(\mathbf{r}'_d, \mathbf{r}_o, \hat{\mathbf{s}}_o) \propto \int_{\mathbb{R}^2} d\mathbf{r}_p\, \mathbf{p}(\mathbf{r}_p, \hat{\mathbf{s}}_o)\exp\left[-2\pi i \frac{n_0}{\lambda f_0}\mathbf{r}_p \cdot \mathbf{r}_o\right]\exp\left[-2\pi i \frac{n_1}{\lambda f_1}\mathbf{r}_p \cdot \mathbf{r}'_d\right]. \tag{44}$$

Note that the Fourier transform of a vector field is the Fourier transform of its scalar-valued orthogonal components, so Eq. (44) specifies three two-dimensional Fourier transforms. We follow the same manipulations as the previous section and find that the dipole coherent transfer function is a scaled dipole pupil function

$$\mathbf{C}(\boldsymbol{\tau}, \hat{\mathbf{s}}_o) \propto \mathbf{p}\left(\frac{\lambda f_o}{n_o}\boldsymbol{\tau}, \hat{\mathbf{s}}_o\right). \tag{45}$$

We have restricted our analysis to paraxial tube lenses, but non-paraxial tube lenses (or a non-infinity-corrected objective) can be modeled with vector-valued three-dimensional pupil functions [26, 29–31].

3.3. Special functions

We adopt and generalize Bracewell's notation [32] for several special functions which will simplify our calculations. First, we define a *rectangle function* as

$$\Pi(x) = \begin{cases} 1 & \text{if } |x| < \frac{1}{2}, \\ 0 & \text{else.} \end{cases} \tag{46}$$

We also define the nth-order jinc function as

$$\text{jinc}_n(r) = \frac{J_{n+1}(\pi r)}{2r}, \tag{47}$$

where $J_{n+1}(r)$ is the $(n+1)^{th}$-order Bessel function of the first kind.

Although the rectangle and jinc functions are defined in one dimension, we will usually apply them in two dimensions. In Appendix B we derive the following two-dimensional Fourier transform relationships between the jinc functions and the weighted rectangle functions

$$i^n \begin{Bmatrix} \exp(in\phi_r) \\ \cos(n\phi_r) \\ \sin(n\phi_r) \end{Bmatrix} \text{jinc}_n(r) \xrightarrow{\mathcal{F}_{\mathbb{R}^2}} (2\nu)^n \begin{Bmatrix} \exp(in\phi_\nu) \\ \cos(n\phi_\nu) \\ \sin(n\phi_\nu) \end{Bmatrix} \Pi(\nu), \tag{48}$$

where the entries inside the curly braces are to be taken one at a time and $\{r, \phi_r\}/\{\nu, \phi_\nu\}$ are conjugate sets of polar coordinates.

Finally, we define the nth-order chat function as the two-dimensional Fourier transform of the squared n^{th}-order jinc function

$$\text{jinc}_n^2(r) \xrightarrow{\mathcal{F}_{\mathbb{R}^2}} \text{chat}_n(\nu). \tag{49}$$

In Appendix B we show that the zeroth- and first-order chat functions can be written in closed form as

$$\text{chat}_0(x) = \frac{1}{2}\left[\cos^{-1}|x| - |x|\sqrt{1-x^2}\right]\Pi\left(\frac{x}{2}\right), \tag{50}$$

$$\text{chat}_1(x) = \frac{1}{2}\left[\cos^{-1}|x| - |x|(3 - 2x^2)\sqrt{1-x^2}\right]\Pi\left(\frac{x}{2}\right). \tag{51}$$

3.4. Monopole transfer functions

Our first step towards the monopole transfer functions is to calculate the monopole pupil function and coherent transfer function. Several works [33, 34] have modeled an aplanatic fluorescence microscope imaging monopole emitters with the scalar pupil function

$$p(\mathbf{r}_P) \propto \tilde{C}\left(\frac{r_p}{f_o}\right)\Pi\left(\frac{r_p}{2f_o \sin\alpha}\right), \tag{52}$$

where

$$\tilde{C}(x) = (1 - x^2)^{-1/4} = 1 + \frac{x^2}{4} + \frac{5x^4}{32} + \cdots . \tag{53}$$

The $\tilde{C}(x)$ function models the radial dependence of the field and ensures that power is conserved on either side of an aplanatic objective, and the rectangle function models the aperture stop of the objective. Applying Eq. (42) and collecting constants we find that the coherent monopole transfer function is

$$C(\tau) \propto \tilde{C}\left(\frac{2\text{NA}}{n_o}\frac{\tau}{\nu_c}\right)\Pi\left(\frac{\tau}{\nu_c}\right), \tag{54}$$

where $\text{NA} = n_o \sin\alpha$ and $\nu_c = 2\text{NA}/\lambda$. This coherent transfer function models objectives with an arbitrary numerical aperture, but for our initial analysis we restrict ourselves to the paraxial regime. We drop second- and higher-order radial terms to find that

$$C(\tau) \overset{(p)}{\propto} \Pi\left(\frac{\tau}{\nu_c}\right), \tag{55}$$

where (p) indicates that we have used the paraxial approximation for the objective lens.

We can find the monopole coherent spread function by taking the inverse Fourier transform of the monopole coherent transfer function

$$c(\mathbf{r}) \overset{(p)}{\propto} \text{jinc}_0(\nu_c r). \tag{56}$$

The monopole point spread function is the (normalized) absolute square of the monopole coherent spread function so

$$h(\mathbf{r}) \overset{(p)}{=} \frac{4}{\pi} \text{jinc}_0^2(\nu_c r), \tag{57}$$

which is the well-known *Airy disk*.

Finally, we can calculate the monopole transfer function as the two-dimensional Fourier transform of the monopole point spread function (or the autocorrelation of the coherent transfer function) and find that

$$H(\nu) \overset{(p)}{=} \frac{4}{\pi} \text{chat}_0\left(\frac{\nu}{\nu_c}\right). \tag{58}$$

3.5. Dipole transfer functions

To calculate the dipole transfer function we proceed similarly to the monopole case—we find the pupil function, scale to find the coherent dipole transfer function, then calculate the remaining transfer functions.

Backer and Moerner [16] have calculated the dipole pupil function for a high-NA objective as

$$\mathbf{p}(\mathbf{r}_p, \hat{\mathbf{s}}_o) \propto \begin{bmatrix} \tilde{C}_0\left(\frac{r_p}{f_o}\right) + \tilde{C}_2\left(\frac{r_p}{f_o}\right)c(2\phi_p) & \tilde{C}_2\left(\frac{r_p}{f_o}\right)s(2\phi_p) & \tilde{C}_1\left(\frac{r_p}{f_o}\right)c(\phi_p) \\ \tilde{C}_2\left(\frac{r_p}{f_o}\right)s(2\phi_p) & \tilde{C}_0\left(\frac{r_p}{f_o}\right) - \tilde{C}_2\left(\frac{r_p}{f_o}\right)c(2\phi_p) & \tilde{C}_1\left(\frac{r_p}{f_o}\right)s(\phi_p) \\ 0 & 0 & 0 \end{bmatrix} \begin{bmatrix} s_x \\ s_y \\ s_z \end{bmatrix} \Pi\left(\frac{r_p}{2f_o s(\alpha)}\right), \tag{59}$$

where $c(x)$ and $s(x)$ are shorthand for $\cos(x)$ and $\sin(x)$, $\{s_x, s_y, s_z\}$ are the Cartesian components of $\hat{\mathbf{s}}_o$ when $\hat{\mathbf{z}}$ is aligned with the optical axis, and

$$\tilde{C}_0(x) = \frac{1}{2}\left(\sqrt{1-x^2}+1\right)(1-x^2)^{-1/4} = 1 + \frac{x^4}{32} + \frac{x^6}{32} + \cdots, \tag{60}$$

$$\tilde{C}_1(x) = x(1-x^2)^{-1/4} \qquad\qquad = x + \frac{x^3}{4} + \frac{5x^5}{32} + \cdots, \tag{61}$$

$$\tilde{C}_2(x) = \frac{1}{2}\left(\sqrt{1-x^2}-1\right)(1-x^2)^{-1/4} = -\frac{x^2}{4} - \frac{x^4}{8} - \frac{11x^6}{128} - \cdots. \tag{62}$$

Similar to the monopole case, the dipole pupil function conserves power and has a cutoff at the objective aperture, but the dipole pupil function is vector-valued to model the complete electric field in the pupil plane. The fields in the pupil plane have a negligible $\hat{\mathbf{z}}$ component which is a consequence of our assumption that the tube lens is paraxial—modeling a non-paraxial tube lens would require a three-dimensional vector-valued pupil function [26, 29–31].

Scaling the dipole pupil function using Eq. (45) yields the dipole coherent transfer function

$$\mathbf{C}(\boldsymbol{\tau}, \hat{\mathbf{s}}_o) \propto \begin{bmatrix} \tilde{C}_0\left(\frac{\lambda r_p \tau}{n_0}\right) + \tilde{C}_2\left(\frac{\lambda r_p \tau}{n_0}\right)c(2\phi_\tau) & \tilde{C}_2\left(\frac{\lambda r_p \tau}{n_0}\right)s(2\phi_\tau) & \tilde{C}_1\left(\frac{\lambda r_p \tau}{n_0}\right)c(\phi_\tau) \\ \tilde{C}_2\left(\frac{\lambda r_p \tau}{n_0}\right)s(2\phi_\tau) & \tilde{C}_0\left(\frac{\lambda r_p \tau}{n_0}\right) - \tilde{C}_2\left(\frac{\lambda r_p \tau}{n_0}\right)c(2\phi_\tau) & \tilde{C}_1\left(\frac{\lambda r_p \tau}{n_0}\right)s(\phi_\tau) \\ 0 & 0 & 0 \end{bmatrix} \begin{bmatrix} s_x \\ s_y \\ s_z \end{bmatrix} \Pi\left(\frac{\tau}{\nu_c}\right). \tag{63}$$

We restrict our analysis to the paraxial regime by dropping second- and higher-order radial terms to find that

$$\mathbf{C}(\tau, \hat{\mathbf{s}}_o) \overset{(p)}{\propto} \begin{bmatrix} 1 & 0 & \frac{2\mathrm{NA}}{n_o} \frac{\tau}{\nu_c} \cos \phi_\tau \\ 0 & 1 & \frac{2\mathrm{NA}}{n_o} \frac{\tau}{\nu_c} \sin \phi_\tau \\ 0 & 0 & 0 \end{bmatrix} \begin{bmatrix} s_x \\ s_y \\ s_z \end{bmatrix} \Pi\left(\frac{\tau}{\nu_c}\right). \tag{64}$$

Under the paraxial approximation the transverse components of the dipole $\{s_x, s_y\}$ create purely transverse fields in the pupil plane and the axial component of the dipole $\{s_z\}$ creates purely radial fields in the pupil plane. The paraxial approximation may seem crude compared to Backer and Moerner's numerical results, but the approximation will allow us to calculate the transfer functions in closed form so that we can build an intuition for the limits of the microscope. We also note that many existing works in ensemble polarized fluorescence microscopy make stronger approximations than ours. For example, Fourkas only considers the total irradiance in the pupil plane while ignoring the propagation of fields to the detector [22].

The dipole coherent spread function is the inverse Fourier transform of the dipole coherent transfer function. Applying Eq. (48) in reverse yields

$$\mathbf{c}(\mathbf{r}, \hat{\mathbf{s}}_o) \overset{(p)}{\propto} \begin{bmatrix} \mathrm{jinc}_0(\nu_c r) & 0 & \frac{\mathrm{NA}}{n_o} i \cos \phi \, \mathrm{jinc}_1(\nu_c r) \\ 0 & \mathrm{jinc}_0(\nu_c r) & \frac{\mathrm{NA}}{n_o} i \sin \phi \, \mathrm{jinc}_1(\nu_c r) \\ 0 & 0 & 0 \end{bmatrix} \begin{bmatrix} s_x \\ s_y \\ s_z \end{bmatrix}. \tag{65}$$

Notice that the radial component of the dipole coherent spread function has a $\pi/2$ phase shift relative to the transverse component. This phase factor arises because the Fourier transform of a real and odd function is purely imaginary.

3.5.1. Paraxial dipole point spread function

The dipole point spread function is the (normalized) absolute square of the coherent dipole spread function

$$h(\mathbf{r}, \hat{\mathbf{s}}_o) \propto \mathbf{c}(\mathbf{r}, \hat{\mathbf{s}}_o) \mathbf{c}^\dagger(\mathbf{r}, \hat{\mathbf{s}}_o). \tag{66}$$

Plugging in the paraxial dipole coherent spread function and normalizing yields

$$h(\mathbf{r}, \hat{\mathbf{s}}_o) \overset{(p)}{=} N\left[\mathrm{jinc}_0^2(\nu_c r) \sin^2 \vartheta + \left(\frac{\mathrm{NA}}{n_o}\right)^2 \mathrm{jinc}_1^2(\nu_c r) \cos^2 \vartheta \right], \tag{67}$$

where $\sin^2 \vartheta = s_x^2 + s_y^2$, $\cos^2 \vartheta = s_z^2$, and the normalization factor is

$$N = 6\nu_c^2 \pi^{-3/2} \left[2 + \left(\frac{\mathrm{NA}}{n_o}\right)^2 \right]^{-1}. \tag{68}$$

As discussed above, the transverse and radial fields are out of phase on the detector, so the total irradiance is the sum of the contributions from the transverse and radial components. In Fig. 6 we plot the dipole point spread function for several dipole orientations and numerical apertures, and in Fig. 7 we compare the monopole point spread function to the dipole point spread function. The paraxial monopole and dipole models are only equivalent when the sample consists of transverse dipoles, which is clear if we notice that Eq. (67) reduces to an Airy disk when $\vartheta = \pi/2$—see Novotny and Hecht for a similar observation [25, ch. 4].
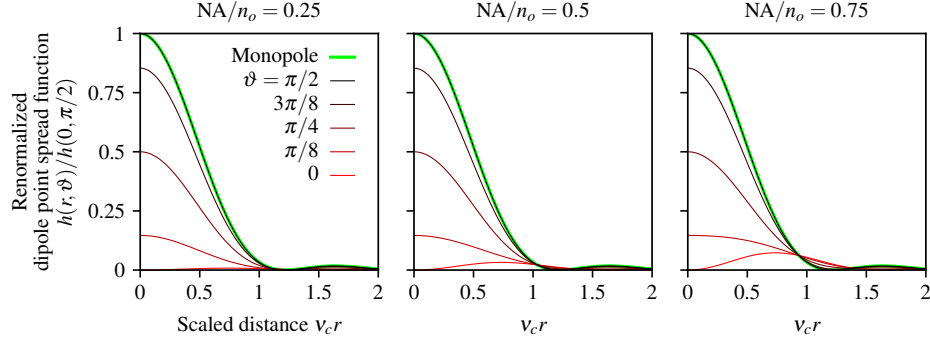
Fig. 6. Renormalized paraxial dipole point spread function as a function of the scaled radial coordinate $v_c r$, the dipole inclination angle ϑ, and NA/n_o. For small numerical apertures (left) the irradiance pattern created by axial dipoles (**red**) is small compared to transverse dipoles (**black**), but the relative contribution of axial dipoles increases with the numerical aperture (see **red** lines from left to right). Additionally, we plot the monopole point spread function (**green**) and observe that the paraxial monopole and dipole models are identical for transverse dipoles (the **green** and **black** lines are coincident).

To demonstrate the paraxial dipole point spread function we simulate a set of equally spaced dipoles with varying orientation:

$$f_{(ph1)}(r_x, r_y, \vartheta, \varphi) = \sum_{j=0}^{3} \sum_{k=0}^{3} \delta(r_x - j)\, \delta(r_y - k)\, \delta(\cos\vartheta - \cos\vartheta_j)\, \delta(\varphi - \varphi_k), \qquad (69)$$

where $\vartheta_j = j\frac{\pi}{6}$, $\varphi_k = k\frac{\pi}{4}$, the subscript $(ph1)$ indicates that this is the first phantom, and the spatial coordinates are expressed in μm. To find the irradiance pattern created by the phantom we plug Eq. (69) into Eq. (19) and use the sifting property to find that

$$g_{(ph1)}(r_x, r_y) = \sum_{j=0}^{3} \sum_{k=0}^{3} h\left(\sqrt{(r_x - j)^2 + (r_y - k)^2}, \vartheta_j\right). \qquad (70)$$

In Fig. 8 we plot the phantom and scaled irradiance for an imaging system with NA = 0.75, $\lambda = 500$ nm, and $n_o = 1.33$. We sample and plot the scaled irradiance at 20× the Nyquist rate, $\Delta x = 1/[20(2v_c)]$, so the irradiance patterns are free of aliasing. The output demonstrates that the irradiance pattern depends on the dipole inclination, but not its azimuth.

3.5.2. Paraxial dipole spatial transfer function

The dipole spatial transfer function is the spatial Fourier transform of the dipole point spread function (or the complex autocorrelation of the dipole coherent transfer function). Applying the Fourier transform to Eq. (67) we find that

$$H(\nu, \vartheta) \stackrel{(p)}{=} \frac{N}{v_c^2} \left[\text{chat}_0\left(\frac{\nu}{v_c}\right) \sin^2\vartheta + \left(\frac{NA}{n_o}\right)^2 \text{chat}_1\left(\frac{\nu}{v_c}\right) \cos^2\vartheta \right]. \qquad (71)$$

In Fig. 9 we plot the dipole spatial transfer function for several dipole orientations and numerical apertures. We find that the dipole spatial transfer function is negative for axial dipoles at high spatial frequencies, especially for larger numerical apertures. The negative dipole spatial transfer
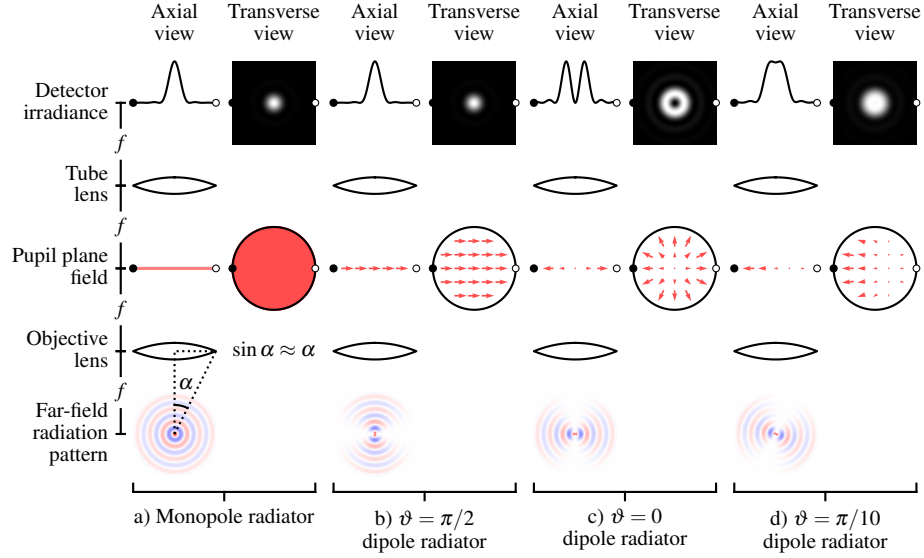
Fig. 7. Comparison of paraxial models for monopole radiators a) and dipole radiators b)–d). a) Monopole radiators fill the pupil plane with a uniform scalar field which gives rise to an Airy disk on the detector. b) A transverse dipole radiator also creates an Airy disk, but the pupil plane is filled with a uniform vector field. c) An axial dipole radiator creates a radial electric field pattern in the back focal plane that creates a $\mathrm{jinc}_1^2(r)$ pattern on the detector. d) Dipoles that are not transverse or axial still create radially symmetric irradiance patterns under the paraxial approximation. Fields from transverse dipoles are real and even while fields from axial dipoles are real and odd, which causes a relative $\pi/2$ phase shift for the fields on the detector. This phase shift means that the fields from transverse and axial components of the dipole do not interfere, which causes radially symmetric irradiance patterns.

corresponds to a contrast inversion for high-frequency patterns of axial dipoles because the irradiance minimum corresponds to the position of the dipole.

To demonstrate the dipole spatial transfer function we simulate a set of equally spaced disks with varying diameter containing fluorophores with varying orientation

$$f_{(ph2)}(r_x, r_y, \vartheta) = \sum_{j=0}^{3} \sum_{k=0}^{3} \frac{1}{D_k^2} \Pi\left(\frac{1}{D_k}\sqrt{(r_x - j)^2 + (r_y - k)^2}\right)\delta\big(\cos\vartheta - \cos\vartheta_j\big) \qquad (72)$$

where $D_k = 0.15(1 + k)\,\mu$m and $\vartheta_j = j\frac{\pi}{6}$. Notice that we have scaled the disks so that the total number of fluorophores in each disk is constant. Also notice that the disk can model a spatial distribution of many fluorophores or a single molecule undergoing spatial diffusion within a well.

We can calculate the irradiance pattern by taking the spatial Fourier transform for each orientation in the phantom, filtering the result with the dipole spatial transfer function, integrating over the orientations, then taking the inverse spatial Fourier transform. Since our phantom is angularly sparse, the integral becomes a sum and we find that

$$g_{(ph2)}(r_x, r_y) = \mathcal{F}_{\mathbb{R}^2}^{-1}\left\{\sum_j H(\nu, \vartheta_j)\mathcal{F}_{\mathbb{R}^2}\big\{f_{(ph2)}(r_x, r_y, \vartheta_j)\big\}\right\}. \qquad (73)$$

In Fig. 10 we plot the phantom and scaled irradiance with the same imaging parameters as the previous section. The small disks create irradiance patterns that are similar to the point sources
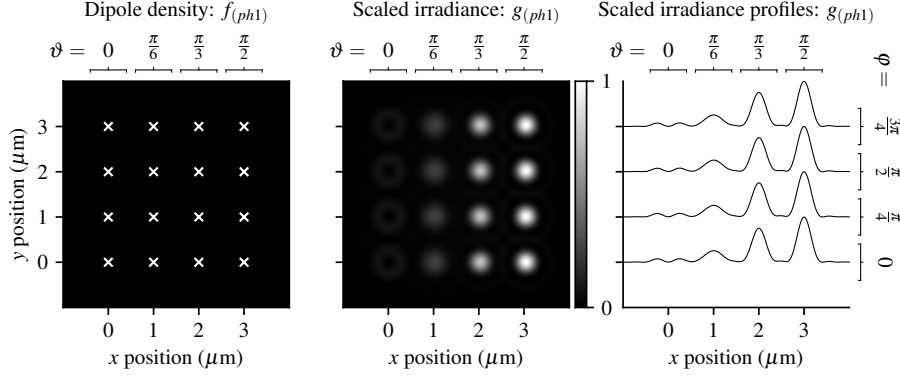
Fig. 8. **Left:** A spatially and angularly sparse phantom—uniformly spaced single dipoles with varying orientations (increasing ϑ from left to right and increasing φ from bottom to top). White crosses mark the positions of the dipoles. **Center:** Scaled irradiance for an imaging system with NA = 0.75, $\lambda = 500$ nm, and $n_o = 1.33$ sampled at 20× the Nyquist rate. **Right:** x profiles through the scaled irradiance. The response is independent of the azimuth angle and strongly dependent on the inclination angle.

in the previous section, while larger disks create increasingly uniform irradiance patterns that hide the orientation of the fluorophores.

3.5.3. Paraxial dipole angular transfer function

To calculate the angular dipole transfer function we take the spherical Fourier transform of the dipole point spread function

$$H_l^m(\mathbf{r}) = \int_{\mathbb{S}^2} d\hat{\mathbf{s}}_o \, h(\mathbf{r}, \hat{\mathbf{s}}_o) Y_l^{m*}(\hat{\mathbf{s}}_o). \tag{74}$$

After evaluating the integrals and normalizing, the angular dipole transfer function is

$$H_l^m(\mathbf{r}) \stackrel{(p)}{=} \frac{N}{3}\left[2\mathrm{jinc}_0^2(\nu_c r) + \left(\frac{\mathrm{NA}}{n_o}\right)^2 \mathrm{jinc}_1^2(\nu_c r)\right]\Lambda_0\delta_{\ell 0}\delta_{m0} +$$

$$\frac{N}{3}\left[-2\mathrm{jinc}_0^2(\nu_c r) + 2\left(\frac{\mathrm{NA}}{n_o}\right)^2 \mathrm{jinc}_1^2(\nu_c r)\right]\Lambda_2\delta_{\ell 2}\delta_{m0}, \tag{75}$$

where $\Lambda_\ell = \sqrt{4\pi/(2\ell + 1)}$.

In Fig. 11 we plot the dipole angular transfer function for both spherical harmonic terms and several numerical apertures. Note that the dipole angular transfer function can be negative because the spherical harmonics can take negative values. The $\ell = 0$ term shows that angularly uniform distributions of dipoles create spatial irradiance patterns that are similar but not identical to the Airy disk, while the $\ell = 2$ term shows a negative pattern because of the large contribution of the transverse negative values in the Y_2^0 spherical harmonic.

To demonstrate the dipole angular transfer function we simulate a set of equally spaced fluorophore distributions with varying orientation and angular distributions

$$f_{(ph3)}(r_x, r_y, \vartheta) = \sum_{j=0}^{3}\sum_{k=0}^{3}\delta(r_x - j)\,\delta(r_y - k)\,f_{(\mathrm{cone})}(\vartheta, \varphi; \vartheta_j, 0, \Delta_k), \tag{76}$$
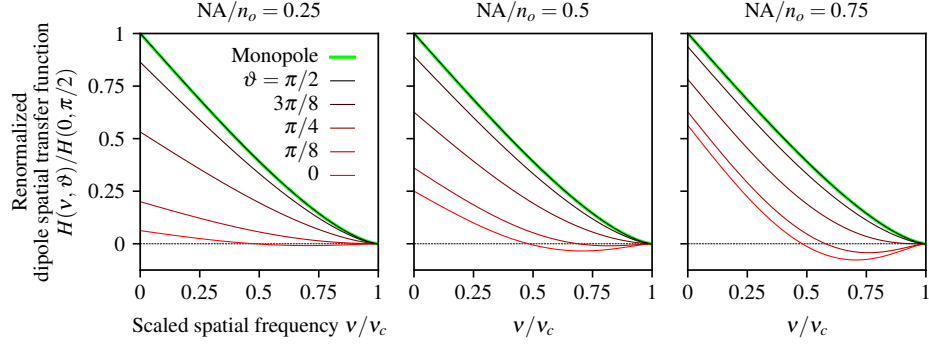
Fig. 9. Dipole spatial transfer function as a function of the scaled spatial frequency ν/ν_c, the dipole inclination angle ϑ, and NA/n_o. For small numerical apertures (left) the dipole spatial transfer function for axial dipoles (**red**) is small compared to transverse dipoles (**black**), but the relative contribution of axial dipoles increases with the numerical aperture (see **red** lines from left to right). The spatial dipole transfer function of axial dipoles is negative at high spatial frequencies because the central minimum of the axial dipole point spread function corresponds to the position of the dipole. Equivalently, a high-spatial-frequency pattern of axial dipoles will generate an irradiance pattern where the minimum irradiance corresponds to the peak of the axial dipole density. Additionally, we plot the monopole transfer function (**green**) and observe that the paraxial monopole and dipole models are identical for transverse dipoles (the **green** and **black** lines are coincident).

where

$$f_{(\text{cone})}(\hat{\mathbf{s}}_o; \hat{\mathbf{s}}_o', \Delta) = f_{(\text{cone})}(\vartheta, \varphi; \vartheta', \varphi', \Delta) = \frac{1}{4\pi(1 - \cos\Delta)}\Pi\left(\frac{\hat{\mathbf{s}} \cdot \hat{\mathbf{s}}'}{2\cos\Delta}\right) \qquad (77)$$

is an angular double cone distribution with central direction $\hat{\mathbf{s}}'$ and cone half-angle Δ; $\vartheta_j = j\frac{\pi}{6}$; and $\Delta_k = k\frac{\pi}{6}$. Notice that when $\Delta = 0$ the angular double cone reduces to a single direction, and when $\Delta = \pi/2$ the angular double cone reduces to an angularly uniform distribution. Also notice that the double cone can model angular diffusion or the angular distribution of many fluorophores within a resolvable volume.

Our first step towards the irradiance pattern is to calculate the dipole angular spectrum of the phantom. In Appendix C we calculate the spherical Fourier transform of the double cone distribution $F_{\ell,(\text{cone})}^m(\vartheta', \varphi'; \Delta)$ which we can use to express the dipole angular spectrum as

$$F_{\ell,(ph3)}^m(r_x, r_y, \vartheta) = \sum_{j=0}^{3}\sum_{k=0}^{3} \delta(r_x - j)\,\delta(r_y - k)\,F_{\ell,(\text{cone})}^m(\vartheta_j, 0, \Delta_k). \qquad (78)$$

To find the irradiance we plug the dipole angular spectrum into Eq. (26) and use the sifting property to find that

$$g_{(ph3)}(r_x, r_y) = \sum_{\ell m}\sum_{j=0}^{3}\sum_{k=0}^{3} H_\ell^m\left(\sqrt{(r_x - j)^2 + (r_y - k)^2}\right)F_{\ell,(\text{cone})}^m(\vartheta_j, 0, \Delta_k). \qquad (79)$$

In Fig. 12 we plot the phantom and scaled irradiance with the same imaging parameters as the previous sections. For small cone angles the irradiance patterns are similar to the point sources in the previous sections, while larger cone angles create increasingly uniform irradiance patterns that hide the angular information about the distributions.
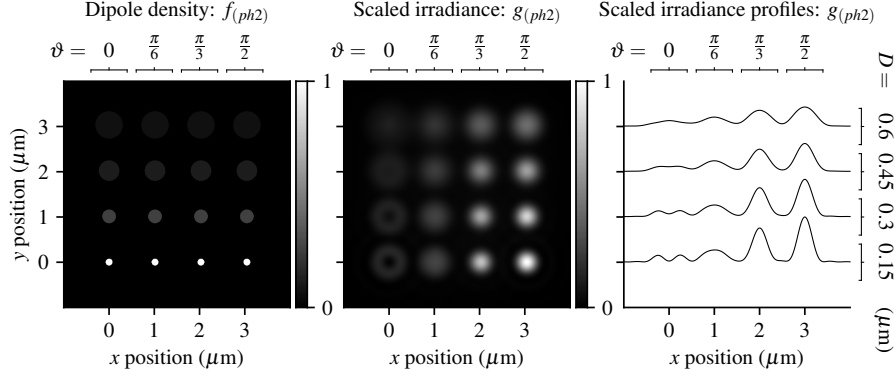
Fig. 10. **Left:** A spatially dense and angularly sparse phantom—uniformly spaced disks with varying size (increasing D from bottom to top) and dipole orientation (increasing ϑ from left to right) **Center:** Scaled irradiance for an imaging system with NA = 0.75, $\lambda = 500$ nm, and $n_o = 1.33$ sampled at 20× the Nyquist rate. **Right:** x profiles through the scaled irradiance. Larger disks generate increasingly uniform irradiance patterns with fewer details that may indicate the orientation of fluorophores.
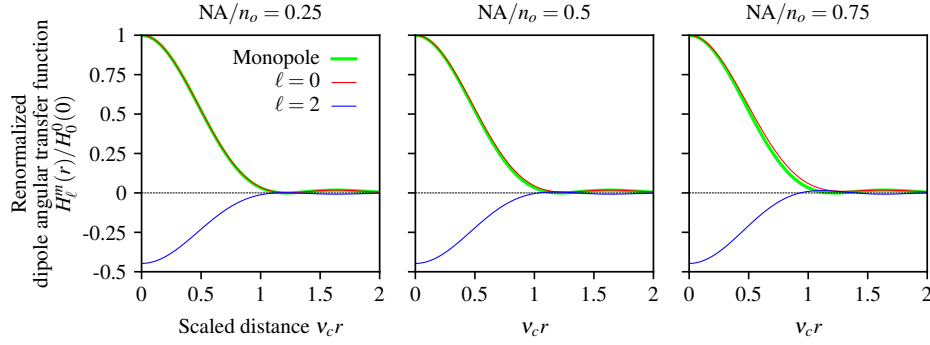
Fig. 11. Paraxial dipole angular transfer function in terms of a scaled radial detection coordinate $v_c r$, the spherical harmonic degree ℓ, and NA/n_o. Angularly uniform distributions of dipoles $\ell = 0$ generate a spatial pattern that is similar but not identical to the Airy disk created by a monopole (**green**), and this discrepancy increases with the numerical aperture. $\ell = 2$ distributions have a negative response because $Y_2^0(\hat{\mathbf{s}})$ is negative for transverse directions. As the numerical aperture increases, the relative contribution of positive axial dipoles in the $\ell = 2$ distribution increases.

3.5.4. Paraxial dipole spatio-angular transfer function

We can calculate the dipole spatio-angular transfer function by taking the spatial Fourier transform of the dipole angular transfer function (or the spherical Fourier transform of the dipole spatial transfer function) to find that

$$
H_\ell^m(\boldsymbol{v}) \stackrel{(p)}{=} \frac{N}{3v_c^2}\left[2\mathrm{chat}_0\left(\frac{v}{v_c}\right) + \left(\frac{\mathrm{NA}}{n_o}\right)^2 \mathrm{chat}_1\left(\frac{v}{v_c}\right)\right]\Lambda_0\delta_{\ell 0}\delta_{m0} +
$$

$$
\frac{N}{3v_c^2}\left[-2\mathrm{chat}_0\left(\frac{v}{v_c}\right) + 2\left(\frac{\mathrm{NA}}{n_o}\right)^2 \mathrm{chat}_1\left(\frac{v}{v_c}\right)\right]\Lambda_2\delta_{\ell 2}\delta_{m0}. \tag{80}
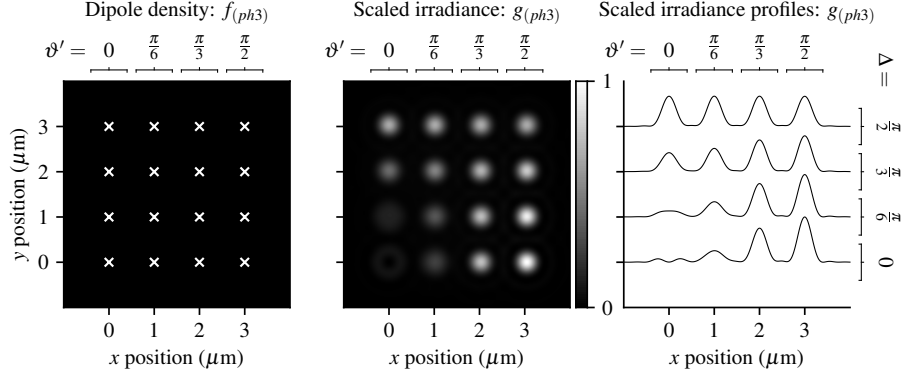$$

Fig. 12. **Left:** A spatially sparse and angularly dense phantom—uniformly spaced double cone distributions of fluorophores with varying central direction (increasing ϑ' from left to right) and varying cone half-angle (increasing Δ from bottom to top). **Center:** Scaled irradiance for an imaging system with NA = 0.75, $\lambda = 500\,\text{nm}$, and $n_o = 1.33$ sampled at $20\times$ the Nyquist rate. **Right:** x profiles through the scaled irradiance. Small cone angles have irradiance patterns that vary with the central direction, while larger cones angles have increasingly uniform irradiance patterns that hide angular information.

In Fig. 13 we plot the dipole spatio-angular transfer function for both spherical harmonic terms and several numerical apertures. The $\ell = 0$ term shows that an angularly uniform distribution of dipoles has a transfer function that is similar but not identical to the monopole transfer function with high frequencies increasingly suppressed as the numerical aperture increases. The $\ell = 2$ term shows a negative pattern because of the large contribution of the transverse negative values in the Y_2^0 spherical harmonic. As the numerical aperture increases the relative contribution of the positive axial values increases and the $\ell = 2$ term becomes less negative.
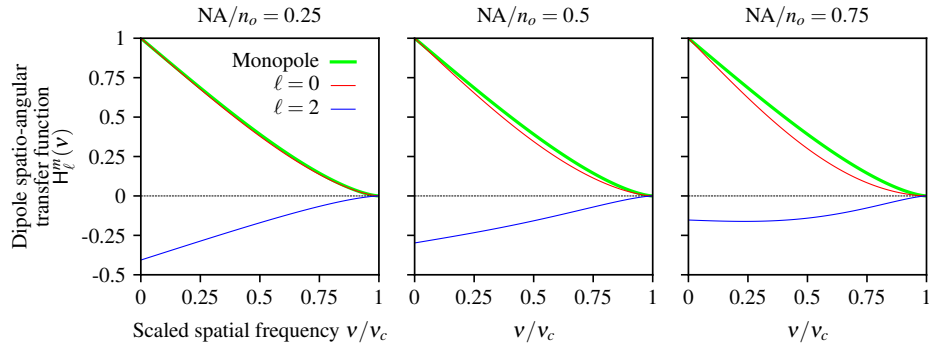

Fig. 13. Spatio-angular dipole transfer function as a function of the scaled spatial frequency ν/ν_c, the spherical harmonic degree ℓ, and NA/n_o. When the numerical aperture is small the transverse dipoles contribute the most to the signal which gives rise to a positive $\ell = 0$ component and a negative $\ell = 2$ component. As the numerical aperture increases, the relative contribution of axial dipoles increases and the $\ell = 2$ component becomes less negative. Additionally, we plot the monopole transfer function (**green**) and observe that the $\ell = 0$ term is similar but not identical to the monopole transfer function, and this discrepancy increases with the numerical aperture.

To demonstrate the spatio-angular transfer function, we simulate a set of equally spaced disks

of fluorophores with varying radius and angular distributions

$$f_{(ph4)}(r_x, r_y, \vartheta, \varphi) = \sum_{j=0}^{3} \sum_{k=0}^{3} \frac{1}{D_k^2} \Pi \left(\frac{1}{D_k} \sqrt{(r_x - j)^2 + (r_y - k)^2} \right) f_{(cone)} \left(\vartheta, \varphi; \frac{\pi}{2}, 0, \Delta_j \right), \quad (81)$$

where $D_k = 0.15(1 + k) \, \mu m$, and $\Delta_j = j \frac{\pi}{6}$.

Our first step towards calculating the irradiance pattern is to calculate the dipole spatio-angular spectrum given by the spatial Fourier transform of the dipole angular spectrum

$$\mathsf{F}_{\ell,(ph4)}^m (\nu_x, \nu_y) = \mathcal{F}_{\mathbb{R}^2} \left\{ \sum_{j=0}^{3} \sum_{k=0}^{3} \frac{1}{D_k^2} \Pi \left(\frac{1}{D_k} \sqrt{(r_x - j)^2 + (r_y - k)^2} \right) \mathsf{F}_{\ell,cone}^m \left(\frac{\pi}{2}, 0, \Delta_j \right) \right\}. \quad (82)$$

We can plug the dipole spatio-angular spectrum into Eq. (29) to find the scaled irradiance as

$$g_{(ph4)}(r_x, r_y) = \mathcal{F}_{\mathbb{R}^2}^{-1} \left\{ \sum_{\ell m} \mathsf{H}_\ell^m (\nu_x, \nu_y) \mathsf{F}_{\ell,(ph4)}^m (\nu_x, \nu_y) \right\}. \quad (83)$$

In Fig. 14 we plot the phantom and scaled irradiance with the same imaging parameters as the previous sections. Small cone angles and small disks create relatively unique irradiance patterns, while increasing the cone angle or disk size creates increasingly similar irradiance patterns.
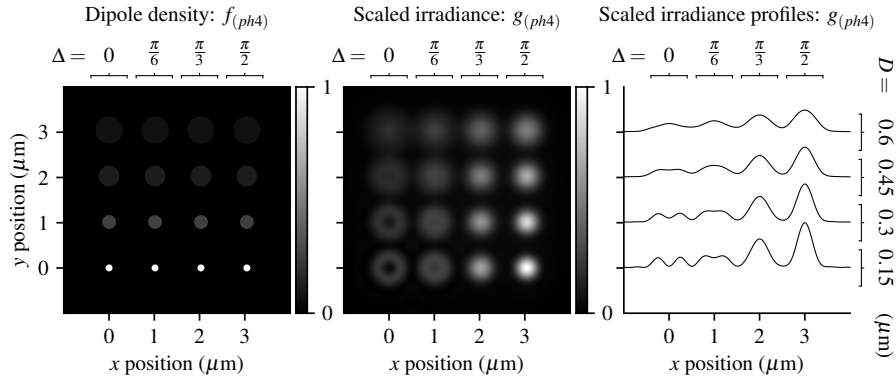

Fig. 14. **Left:** A spatially and angularly dense phantom—uniformly spaced disks with varying size (increasing D from bottom to top) and double cone half angle (increasing Δ from left to right) **Center:** Scaled irradiance for an imaging system with NA = 0.75, $\lambda = 500$ nm, and $n_o = 1.33$ sampled at 20× the Nyquist rate. **Right:** x profiles through the scaled irradiance.

4. Discussion

4.1. When are dipole transfer functions necessary?

Model mismatch can lead to biased estimates of the position and orientation of fluorophores, so the most accurate fluorescence microscopy experiments will always use dipole transfer functions over monopole transfer functions. The only case when the dipole and monopole transfer functions match exactly is when the dipoles are completely constrained to the transverse plane of a paraxial imaging system.

However, in many practical situations noise will mask the effects of vector optics and dipoles. If the fluorophores are rotationally unconstrained or there are many randomly oriented fluorophores

in a resolvable volume—common situations in biological applications—then the effects of vector optics and dipoles will be masked by noise in all but the highest-SNR regimes.

The dipole transfer functions are most broadly useful when the sample contains fluorophores that are rotationally constrained. As rotational constraints increase, the effects of vector optics and dipoles will become apparent in lower SNR regimes.

4.2. Alternative transfer functions

Throughout this work we have used the spherical harmonic functions as a basis for functions on the sphere, but there are other basis functions that can be advantageous in some cases. Several works [7, 15, 16, 18, 35] have used the second moments as basis functions for the sphere because they arise naturally when computing the dipole point spread function. These works use an alternative to the dipole angular transfer function that uses the second moments as basis functions so the forward model can be written as

$$g(\mathbf{r}_d) = \sum_{j=1}^{6} \int_{\mathbb{R}^2} d\mathbf{r}_o \, H_j(\mathbf{r}_d - \mathbf{r}_o) F_j(\mathbf{r}_o), \tag{84}$$

where

$$H_j(\mathbf{r}_d - \mathbf{r}_o) = \int_{\mathbb{S}^2} d\hat{\mathbf{s}}_o \, h(\mathbf{r}_d - \mathbf{r}_o, \hat{\mathbf{s}}_o) Z_j(\hat{\mathbf{s}}_o), \tag{85}$$

$$F_j(\mathbf{r}_o) = \int_{\mathbb{S}^2} d\hat{\mathbf{s}}_o \, f(\mathbf{r}_o, \hat{\mathbf{s}}_o) Z_j(\hat{\mathbf{s}}_o), \tag{86}$$

and $Z_j(\hat{\mathbf{s}}) = \{s_x^2, s_y^2, s_z^2, s_x s_y, s_y s_z, s_x s_z\}$ are the second moments. This formulation is similar to the dipole angular transfer function approach because it can exploit the spatial sparsity of the sample, but it does not require a cumbersome expansion of the dipole point spread function onto spherical harmonics.

However, the spherical harmonics provide several advantages over the second moments. First, the spherical harmonics form a complete basis for functions on the sphere, while the second moments span a much smaller function space. The usual approach to extending the span of the second moments is to use the fourth (or higher) moments, but this extension requires a completely new set of basis functions while the spherical harmonics can be extended by simply adding higher order terms. Second, the spherical harmonics are orthonormal, which will allow us to deploy invaluable tools from linear algebra—linear subspaces, rank, decompositions, etc.— to analyze and compare microscope designs. Finally, using the spherical harmonics provides access to a set of fast algorithms. The naive expansion of an arbitrary discretized N point spherical function onto spherical harmonics (or second moments) requires a $\mathcal{O}(N^2)$ matrix multiplication, while pioneering work by Driscoll and Healy [36] showed that the forward discrete fast spherical harmonic transform can be computed with a $\mathcal{O}(N(\log N)^2)$ algorithm and its inverse can be computed with a $\mathcal{O}(N^{3/2})$ algorithm. To our knowledge no similarly fast algorithms exist for expansion onto the higher-order moments.

Zhenghao et. al. [5] have used the circular harmonics to model the orientation of dipoles. The circular harmonics are complete and orthogonal, but they artificially restrict the reconstructed dipoles to the transverse plane of the microscope—a rare situation in real experiments.

The diffusion magnetic resonance imaging community uses both the second moments (or second-order tensor) basis functions [37] and the spherical harmonic basis functions [38]. Descoteaux et. al. have provided an explicit transformation matrix to convert between these basis functions [39].

4.3. What determines the angular bandwidth?

Spatial imaging systems have a spatial bandwidth that characterizes the highest spatial frequency that the system can image. Similarly, angular imaging systems have an angular bandwidth that characterizes the highest angular frequency that the system can image, but in the angular case there are two different types of angular bandwidths that we call the ℓ- and m-bandwidth. The ℓ-bandwidth can be interpreted in a similar way to the spatial bandwidth—it characterizes the smallest angular features that the imaging system can measure. The m-bandwidth does not have a direct analog in the spatial domain—it characterizes the angular uniformity of the imaging system. If the ℓ- and m-bandwidths are equal then the imaging system can be said to have an *isotropic angular bandwidth*.

The spatial bandwidth of a fluorescence microscope is well known to be $\nu_c = \frac{2\text{NA}}{\lambda}$. In other words, we can increase the spatial resolution of a fluorescence microscope by increasing the NA of the instrument or by choosing a fluorophore with a shorter emission wavelength. Similarly, the angular bandwidth of a fluorescence microscope depends on both the instrument and the sample.

The microscope we considered in this work has an ℓ-bandwidth of $\ell_c = 2$ and an m-bandwidth of $m_c = 0$, so it does not have an isotropic angular bandwidth. In future work we will consider several approaches to improving the angular bandwidths in detail, but we briefly mention that non-paraxial microscopes, microscopes with polarizers on the illumination or detection paths, and multiview microscopes all have higher angular bandwidths than the microscope considered here.

The angular bandwidth is also sample dependent. Monopoles emit light isotropically so they have an ℓ-bandwidth of $\ell_c = 0$, while dipoles have an ℓ-bandwidth of $\ell_c = 2$, and higher-order excitation and detection moments will have even higher bandwidths. Multi-photon excitation and other non-linear methods can also increase the ℓ-bandwidth [35].

4.4. Towards more realistic models

The theoretical model we presented in this work is an extreme simplification of a real microscope. We have ignored the effects of thick samples, refractive-index mismatch, aberration, scattering, finite fluorescence lifetimes, and interactions between fluorophores among others. Because of this long list of unknown effects, real experiments will likely require extensions of the models developed here.

The dipole pupil function provides the simplest way to create more realistic models from the simple model in this paper. Phase aberrations can be added to the dipole pupil function with Zernike polynomials, and refractive index boundaries can be modeled by applying the work of Gibson and Lanni to the dipole pupil function [20]. These additions will model phase aberrations, but modeling polarization aberrations will also be necessary, and we anticipate that vector Zernike polynomials and the Jones pupil [40–42] will be essential tools for modeling dipole imaging systems. We plan to use the dipole pupil function to include the effects of non-paraxial objectives, polarizers, and defocus in future papers of this series.

The dipole pupil function also provides an enormous set of design opportunities. The dipole imaging problem may benefit from spatially varying diattenuating and birefrigent masks—a much larger set of possibilities than the well-explored design space of amplitude and phase masks. The dipole pupil function is a step towards Green's tensor engineering [6], and the dipole transfer functions provide a strong framework for evaluating dipole imaging designs.

In the simple case considered here we focused on the emission path of the microscope, but the excitation path is equally important. Complete models will need to consider the spatio-angular dependence of excitation. Zhenghao et. al. [5] have taken steps in this direction by considering polarized structured illumination microscopy. Rotational dynamics and the fluorescence lifetime are also important to consider when incorporating models of the excitation process [7, 11, 18].

4.5. Towards spatio-angular reconstructions

We have focused on modeling the mapping between the object and the data in this paper, but ultimately we are interested in reconstructing the object from the data. Applying the monopole approximation simplifies the reconstruction problem because both object and data space are $\mathbb{L}_2(\mathbb{R}^2)$, so we can directly apply regularized inverse filters and maximum likelihood methods. The dipole model expands object space to $\mathbb{L}_2(\mathbb{R}^2 \times \mathbb{S}^2)$, so the inverse problem becomes much more challenging. In future work we will use the singular value decomposition to find inverse filters, and we will consider using polarizers and multiple views to increase the size of data space.

5. Conclusions

Many models of fluorescence microscopes use the monopole and scalar approximations, but complete models need to consider dipole and vector optics effects. We have introduced several transfer functions that simplify the mapping between the dipole density and the irradiance pattern on the detector, and we have demonstrated these transfer functions by efficiently simulating a paraxial fluorescence microscope. We found that the monopole and scalar approximations are good approximations when the sample consists of unconstrained rotating fluorophores or many randomly oriented fluorophores within a resolvable volume. We also found that dipole and vector optics effects become larger as rotational order increases, and in these cases the dipole transfer functions become valuable tools.

Disclosures

The authors declare that there are no conflicts of interest related to this article.

References

1. A. M. Vrabioiu and T. J. Mitchison, "Structural insights into yeast septin organization from polarized fluorescence microscopy," Nature **443**, 466–469 (2006).
2. A. L. Mattheyses, M. Kampmann, C. E. Atkinson, and S. M. Simon, "Fluorescence anisotropy reveals order and disorder of protein domains in the nuclear pore complex," Biophys. J. **99**, 1706–1717 (2010).
3. S. B. Mehta, M. McQuilken, P. J. La Rivière, P. Occhipinti, A. Verma, R. Oldenbourg, A. S. Gladfelter, and T. Tani, "Dissection of molecular assembly dynamics by tracking orientation and position of single molecules in live cells," Proc. Natl. Acad. Sci. U.S.A. **113**, E6352–E6361 (2016).
4. M. McQuilken, M. S. Jentzsch, A. Verma, S. B. Mehta, R. Oldenbourg, and A. S. Gladfelter, "Analysis of septin reorganization at cytokinesis using polarized fluorescence microscopy," Front. Cell Dev. Biol. **5**, 42 (2017).
5. K. Zhanghao, X. Chen, W. Liu, M. Li, C. Shan, X. Wang, K. Zhao, A. Lai, H. Xie, Q. Dai, and P. Xi, "Structured illumination in spatial-orientational hyperspace," https://arxiv.org/abs/1712.05092 .

6. A. Agrawal, S. Quirin, G. Grover, and R. Piestun, "Limits of 3D dipole localization and orientation estimation for single-molecule imaging: towards Green's tensor engineering," Opt. Express **20**, 26667–26680 (2012).

7. O. Zhang, J. Lu, T. Ding, and M. D. Lew, "Imaging the three-dimensional orientation and rotational mobility of fluorescent emitters using the tri-spot point spread function," Appl. Phys. Lett. **113**, 031103 (2018).

8. M. R. Foreman and P. Török, "Fundamental limits in single-molecule orientation measurements," New J. Phys. **13**, 093013 (2011).

9. J. Chao, E. S. Ward, and R. J. Ober, "Fisher information theory for parameter estimation in single molecule microscopy: tutorial," J. Opt. Soc. Am. A **33**, B36–B57 (2016).

10. M. P. Backlund, M. D. Lew, A. S. Backer, S. J. Sahl, and W. E. Moerner, "The role of molecular dipole orientation in single-molecule fluorescence microscopy and implications for super-resolution imaging," ChemPhysChem **15**, 587–599 (2014).

11. M. D. Lew, M. P. Backlund, and W. E. Moerner, "Rotational mobility of single molecules affects localization accuracy in super-resolution fluorescence microscopy," Nano Lett. **13**, 3967–3972 (2013).

12. M. Böhmer and J. Enderlein, "Orientation imaging of single molecules by wide-field epifluorescence microscopy," J. Opt. Soc. Am. B **20**, 554–559 (2003).

13. M. A. Lieb, J. M. Zavislan, and L. Novotny, "Single-molecule orientations determined by direct emission pattern imaging," J. Opt. Soc. Am. B **21**, 1210–1215 (2004).

14. E. Toprak, J. Enderlein, S. Syed, S. A. McKinney, R. G. Petschek, T. Ha, Y. E. Goldman, and P. R. Selvin, "Defocused orientation and position imaging (DOPI) of myosin V," Proc. Natl. Acad. Sci. U.S.A. **103**, 6495–6499 (2006).

15. F. Aguet, S. Geissbühler, I. Märki, T. Lasser, and M. Unser, "Super-resolution orientation estimation and localization of fluorescent dipoles using 3-D steerable filters," Opt. Express **17**, 6829–6848 (2009).

16. A. S. Backer and W. E. Moerner, "Extending single-molecule microscopy using optical Fourier processing," J. Phys. Chem. B **118**, 8313–8329 (2014).

17. S. Stallinga, "Effect of rotational diffusion in an orientational potential well on the point spread function of electric dipole emitters," J. Opt. Soc. Am. A **32**, 213–223 (2015).

18. O. Zhang and M. D. Lew, "Fundamental limits on measuring the rotational constraint of single molecules using fluorescence microscopy," https://arxiv.org/abs/1811.09017 .

19. M. Born and E. Wolf, *Principles of Optics: Electromagnetic Theory of Propagation, Interference and Diffraction of Light* (Elsevier Science Limited, 1980).

20. S. F. Gibson and F. Lanni, "Diffraction by a circular aperture as a model for three-dimensional optical microscopy," J. Opt. Soc. Am. A **6**, 1357–1367 (1989).

21. B. Richards and E. Wolf, "Electromagnetic diffraction in optical systems, II. structure of the image field in an aplanatic system," Proc. Royal Soc. Lond. A: Math. Phys. Eng. Sci. **253**, 358–379 (1959).

22. J. T. Fourkas, "Rapid determination of the three-dimensional orientation of single molecules," Opt. Lett. **26**, 211–213 (2001).

23. H. Barrett and K. Myers, *Foundations of Image Science* (Wiley-Interscience, 2004).

24. M. Mansuripur, *Classical Optics and Its Applications* (Cambridge University Press, 2009).

25. L. Novotny and B. Hecht, *Principles of Nano-Optics* (Cambridge University Press, 2006).

26. M. Gu, *Advanced Optical Imaging Theory*, Springer Series in Optical Sciences (Springer, 2000).

27. J. Goodman, *Introduction to Fourier Optics* (McGraw-Hill, 1996).

28. D. Axelrod, "Fluorescence excitation and imaging of single molecules near dielectric-coated and bare surfaces: a theoretical study." J. Microsc. **247 2**, 147–60 (2012).

29. C. J. R. Sheppard, M. Gu, Y. Kawata, and S. Kawata, "Three-dimensional transfer functions for high-aperture systems," J. Opt. Soc. Am. A **11**, 593–598 (1994).

30. M. R. Arnison and C. J. Sheppard, "A 3D vectorial optical transfer function suitable for arbitrary pupil functions," Opt. Commun. **211**, 53–63 (2002).

31. M. R. Foreman and P. Török, "Computational methods in vectorial imaging," J. Mod. Opt. **58**, 339–364 (2011).

32. R. Bracewell, *Fourier Analysis and Imaging* (Springer US, 2004).

33. P. N. Petrov, Y. Shechtman, and W. E. Moerner, "Measurement-based estimation of global pupil functions in 3D localization microscopy," Opt. Express **25**, 7945–7959 (2017).

34. M. P. Backlund, Y. Shechtman, and R. L. Walsworth, "Fundamental precision bounds for three-dimensional optical localization microscopy with Poisson statistics," Phys. Rev. Lett. **121**, 023904 (2018).

35. S. Brasselet, "Polarization-resolved nonlinear microscopy: application to structural molecular and biological imaging," Adv. Opt. Photon. **3**, 205 (2011).

36. J. Driscoll and D. Healy, "Computing Fourier transforms and convolutions on the 2-sphere," Adv. Appl. Math. **15**, 202–250 (1994).

37. P. Basser, J. Mattiello, and D. LeBihan, "MR diffusion tensor spectroscopy and imaging," Biophys. J. **66**, 259–267 (1994).

38. J.-D. Tournier, F. Calamante, D. G. Gadian, and A. Connelly, "Direct estimation of the fiber orientation density function from diffusion-weighted MRI data using spherical deconvolution," NeuroImage **23**, 1176 – 1185 (2004).

39. M. Descoteaux, E. Angelino, S. Fitzgibbons, and R. Deriche, "Apparent diffusion coefficients from high angular resolution diffusion imaging: estimation and applications," Magn. Reson. Medicine **56**, 395–410 (2006).

40. C. Zhao and J. H. Burge, "Orthonormal vector polynomials in a unit circle, part I: basis set derived from gradients of

Zernike polynomials," Opt. Express **15**, 18014–18024 (2007).

41. X. Xu, W. Huang, and M. Xu, "Orthogonal polynomials describing polarization aberration for rotationally symmetric optical systems," Opt. Express **23**, 27911–27919 (2015).

42. R. A. Chipman, "Polarization analysis of optical systems," Opt. Eng. **28**, 28 – 28 – 10 (1989).

43. N. Schaeffer, "Efficient spherical harmonic transforms aimed at pseudospectral numerical simulations," Geochem. Geophys. Geosystems **14**, 751–758 (2013).

44. I. S. Gradshteyn and I. M. Ryzhik, *Table of Integrals, Series, and Products* (Elsevier/Academic Press, Amsterdam, 2007).

45. J. Mertz, *Introduction to Optical Microscopy* (W. H. Freeman, 2009).

46. R. Ramamoorthi, "Modeling illumination variation with spherical harmonics," in *Face Processing: Advanced Modeling and Methods,* (Academic Press, 2005).

A. Spherical harmonics and the spherical Fourier transform

The spherical harmonic function of degree ℓ and order $-\ell \le m \le \ell$ is defined as [43]

$$Y_\ell^m(\vartheta, \varphi) = \sqrt{\frac{2\ell + 1}{4\pi}} \sqrt{\frac{(\ell - |m|)!}{(\ell + |m|)!}} P_\ell^m(\cos \vartheta) \exp(im\varphi), \tag{87}$$

where $P_\ell^m(\cos \vartheta)$ are the associated Legendre polynomials with the Condon-Shortley phase

$$P_\ell^m(x) = (-1)^m (1 - x^2)^{|m|/2} \frac{d^{|m|}}{dx^{|m|}} P_\ell(x), \tag{88}$$

and $P_\ell(x)$ are the Legendre polynomials defined by the recurrence

$$P_0(x) = 1, \tag{89}$$
$$P_1(x) = x, \tag{90}$$
$$\ell P_\ell(x) = (2\ell - 1)x P_{\ell-1}(x) - (\ell - 1)P_{\ell-2}(x). \tag{91}$$

The spherical harmonics are orthonormal, which means that

$$\int_{\mathbb{S}^2} d\hat{\mathbf{s}} \, Y_\ell^m(\hat{\mathbf{s}}) Y_{\ell'}^{m'*}(\hat{\mathbf{s}}) = \delta_{\ell\ell'} \delta_{mm'}, \tag{92}$$

where $\delta_{\ell\ell'}$ denotes the Kronecker delta. The spherical harmonics form a complete basis, so an arbitrary function on the sphere $f(\hat{\mathbf{s}})$ can be expanded into a sum of weighted spherical harmonic functions

$$f(\hat{\mathbf{s}}) = \sum_{\ell=0}^{\infty} \sum_{m=-\ell}^{l} F_\ell^m Y_\ell^m(\hat{\mathbf{s}}). \tag{93}$$

We can find the spherical harmonic coefficients F_ℓ^m for a given function using Fourier's trick—multiply both sides by $Y_\ell^{m*}(\hat{\mathbf{s}})$, integrate over the sphere, and exploit orthogonality to find that

$$F_\ell^m = \int_{\mathbb{S}^2} d\hat{\mathbf{s}} \, f(\hat{\mathbf{s}}) Y_\ell^{m*}(\hat{\mathbf{s}}). \tag{94}$$

The coefficients F_ℓ^m are called the *spherical Fourier transform* of a spherical function.

B. Relationships between special functions

Our first task is to show that

$$i^n \begin{Bmatrix} \exp(in\phi_r) \\ \cos(n\phi_r) \\ \sin(n\phi_r) \end{Bmatrix} \mathrm{jinc}_n(r) \xrightarrow{\mathcal{F}_{\mathbb{R}^2}} (2\nu)^n \begin{Bmatrix} \exp(in\phi_\nu) \\ \cos(n\phi_\nu) \\ \sin(n\phi_\nu) \end{Bmatrix} \Pi(\nu). \tag{95}$$

Writing the inverse Fourier transform in polar coordinates yields

$$= 2^n \int_0^{1/2} d\nu \, \nu^{n+1} \int_0^{2\pi} d\phi_\nu \begin{Bmatrix} \exp(in\phi_\nu) \\ \cos(n\phi_\nu) \\ \sin(n\phi_\nu) \end{Bmatrix} \exp[2\pi i\nu r \cos(\phi_\nu - \phi_r)]. \tag{96}$$

The azimuthal integral can be evaluated in terms of an nth order Bessel function (for the complex case see [23, ch. 4.111]).

$$= 2^n 2\pi i^n \begin{Bmatrix} \exp(in\phi_r) \\ \cos(n\phi_r) \\ \sin(n\phi_r) \end{Bmatrix} \int_0^{1/2} d\nu \, \nu^{n+1} J_n(2\pi\nu r). \tag{97}$$

We can use the following identity [44, ch. 6.561-5]

$$\int_0^1 du \, u^{n+1} J_n(au) = a^{-1} J_{n+1}(a) \tag{98}$$

with a change of variable $u = 2\nu$ to find the final result

$$= 2^n 2\pi i^n \begin{Bmatrix} \exp(in\phi_r) \\ \cos(n\phi_r) \\ \sin(n\phi_r) \end{Bmatrix} \int_0^1 \frac{du}{2} \left(\frac{u}{2}\right)^{n+1} J_n(\pi u r) = i^n \begin{Bmatrix} \exp(in\phi_r) \\ \cos(n\phi_r) \\ \sin(n\phi_r) \end{Bmatrix} \frac{J_{n+1}(\pi r)}{2r} = i^n \begin{Bmatrix} \exp(in\phi_r) \\ \cos(n\phi_r) \\ \sin(n\phi_r) \end{Bmatrix} \mathrm{jinc}_n(r). \tag{99}$$
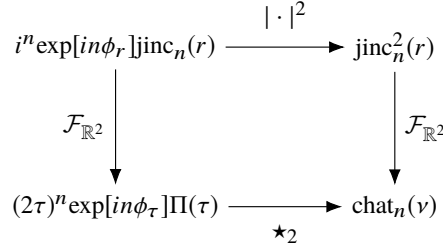

Fig. 15. The relationships between special functions. The chat functions are defined as the two-dimensional Fourier transform of the squared jinc functions, and they can be calculated with the two-dimensional complex autocorrelations (denoted by $\star_2$) of the complex-weighted rectangle functions.

We can use the relationship in Eq. (95) to express the chat functions in terms of a complex autocorrelation—see the diagram in Fig. 15. Starting with the definition of the nth-order chat function

$$\mathrm{chat}_n(\nu) = \int_{\mathbb{R}^2} d\mathbf{r} \, \mathrm{jinc}_n^2(|\mathbf{r}|) \exp[-2\pi i \mathbf{r}\nu], \tag{100}$$

we can rewrite the integrand in terms of the absolute square of a simpler function with a known Fourier transform

$$\mathrm{chat}_n(\nu) = \int_{\mathbb{R}^2} d\mathbf{r} \, |t_n(\mathbf{r})|^2 \exp[-2\pi i \mathbf{r}\nu]. \tag{101}$$

$$t_n(\mathbf{r}) = i^n \exp[in\phi_r] \mathrm{jinc}_n(r). \tag{102}$$

Now we can apply the autocorrelation theorem to rewrite the Fourier transform as

$$\mathrm{chat}_n(\nu) = \int_{\mathbb{R}^2} d\tau \, T_n(\tau) T_n^*(\tau - \nu), \tag{103}$$

where the function to be autocorrelated can be found with the help of Eq. (95)

$$T_n(\boldsymbol{\tau}) = \int_{\mathbb{R}^2} d\mathbf{r}\, t_n(\mathbf{r}) \exp[-2\pi i \mathbf{r} \cdot \boldsymbol{\tau}] = (2\tau)^n \exp[in\phi_\tau]\Pi(\tau). \tag{104}$$

It will be more convenient to set up the autocorrelation in Cartesian coordinates

$$T_n(\boldsymbol{\tau}) = 2^n (\tau_x + i\tau_y)^n \Pi\left(\sqrt{\tau_x^2 + \tau_y^2}\right). \tag{105}$$

Plugging Eq. (105) into Eq. (103) gives

$$\mathrm{chat}_n(v) = 4^n \int_{\mathbb{R}^2} d\boldsymbol{\tau}\, (\tau_x^2 + \tau_y^2 - v\tau_x)^n \Pi\left(\sqrt{\tau_x^2 + \tau_y^2}\right)\Pi\left(\sqrt{(\tau_x - v)^2 + \tau_y^2}\right). \tag{106}$$

We can interpret the autocorrelation as an integral over a region of overlap between a circle centered at the origin and a circle shifted to the right by v (a geometric lens). Using the construction in Fig. 16 we can express this region as

$$\mathrm{chat}_n(v) = 4^{n+1}\left[\int_0^{1/2} \tau d\tau \int_0^{\cos^{-1} v} d\phi_\tau (\tau^2 - v\tau \cos\phi_\tau)^n - \right.$$
$$\left. \int_0^{v/2} d\tau_x \int_0^{\frac{\tau_x}{v}\sqrt{1-v^2}} d\tau_y (\tau_x^2 + \tau_y^2 - v\tau_x)^n \right]\Pi\left(\frac{v}{2}\right). \tag{107}$$
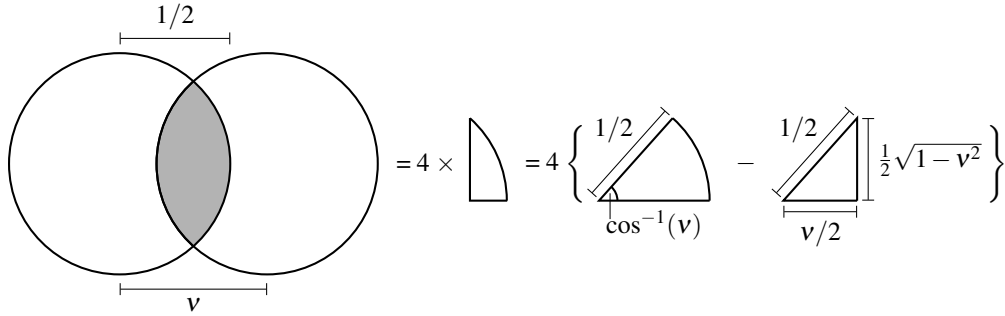

Fig. 16. Geometric construction for evaluating the autocorrelation. We need to integrate over the overlapping region of two circles with radius $1/2$ and distance v between their centers. The region is four times the difference in area between a sector of angle $\cos^{-1}(v)$ and radius $1/2$ and a right triangle with base $v/2$ and hypotenuse $1/2$.

For $n = 0$:

$$\mathrm{chat}_0(v) = 4\left[\int_0^{1/2} \tau d\tau \int_0^{\cos^{-1} v} d\phi_\tau - \int_0^{v/2} d\tau_x \int_0^{\frac{\tau_x}{v}\sqrt{1-v^2}} d\tau_y \right]\Pi\left(\frac{v}{2}\right), \tag{108}$$

$$\mathrm{chat}_0(v) = \frac{1}{2}\left[\cos^{-1}|v| - |v|\sqrt{1-v^2} \right]\Pi\left(\frac{v}{2}\right), \tag{109}$$

which is a well-known result [27, 32, 45]. For $n = 1$:

$$\mathrm{chat}_1(\nu) = 16 \left[\int_0^{1/2} \tau d\tau \int_0^{\cos^{-1}\nu} d\phi_\tau (\tau^2 - \nu\tau \cos\phi_\tau) - \right.$$
$$\left. \int_0^{\nu/2} d\tau_x \int_0^{\frac{\tau_x}{\nu}\sqrt{1-\nu^2}} d\tau_y \, (\tau_x^2 + \tau_y^2 - \nu\tau_x) \right] \Pi\left(\frac{\nu}{2}\right), \tag{110}$$

$$\mathrm{chat}_1(\nu) = \frac{1}{2}\left[\cos^{-1}|\nu| - |\nu|(3 - 2\nu^2)\sqrt{1 - \nu^2} \right] \Pi\left(\frac{\nu}{2}\right). \tag{111}$$

C. Spherical Fourier transform of a double cone

In this appendix we evaluate the spherical Fourier transform of a normalized double-cone angular distribution with central direction $\hat{\mathbf{s}}'$ and cone half-angle Δ

$$f_{(\mathrm{cone})}(\hat{\mathbf{s}}; \hat{\mathbf{s}}', \Delta) = \frac{1}{4\pi(1 - \cos\Delta)} \Pi\left(\frac{\hat{\mathbf{s}} \cdot \hat{\mathbf{s}}'}{2\cos\Delta} \right). \tag{112}$$

The spherical Fourier transform is

$$F^m_{\ell(\mathrm{cone})}(\hat{\mathbf{s}}', \Delta) = \int_{\mathbb{S}^2} d\hat{\mathbf{s}} \, f_{(\mathrm{cone})}(\hat{\mathbf{s}}; \hat{\mathbf{s}}', \Delta) Y^{m*}_\ell(\hat{\mathbf{s}}). \tag{113}$$

The limits of integration will be difficult to find unless we change coordinates to exploit the axis of symmetry $\hat{\mathbf{s}}'$. Since the spherical function is rotationally symmetric about $\hat{\mathbf{s}}'$ we can rotate the function so that the axis of symmetry is aligned with $\hat{\mathbf{z}}$ and multiply by $\sqrt{\frac{4\pi}{2l+1}} Y^{m*}_\ell(\hat{\mathbf{s}}')$ to account for the rotation [46]

$$F^m_{\ell(\mathrm{cone})}(\hat{\mathbf{s}}', \Delta) = \sqrt{\frac{4\pi}{2l + 1}} Y^{m*}_\ell(\hat{\mathbf{s}}') \int_{\mathbb{S}^2} d\hat{\mathbf{s}} \, f_{(\mathrm{cone})}(\vartheta; \hat{\mathbf{z}}, \Delta) Y^0_\ell(\hat{\mathbf{s}}). \tag{114}$$

In this coordinate system the double cone is independent of the azimuthal angle, so we can evaluate the azimuthal integral and express the function in terms of an integral over ϑ:

$$F^m_{\ell(\mathrm{cone})}(\hat{\mathbf{s}}', \Delta) = 2\pi Y^{m*}_\ell(\hat{\mathbf{s}}') \int_0^\pi d\vartheta \, \sin\vartheta f_{(\mathrm{cone})}(\vartheta; \hat{\mathbf{z}}, \Delta) P_\ell(\cos\vartheta). \tag{115}$$

The function $f_{(\mathrm{cone})}(\vartheta; \hat{\mathbf{z}}, \Delta)$ is only non-zero on the intervals $\vartheta \in [0, \Delta]$ and $\vartheta \in [\pi - \Delta, \pi]$ so

$$F^m_{\ell(\mathrm{cone})}(\hat{\mathbf{s}}', \Delta) = \frac{Y^{m*}_\ell(\hat{\mathbf{s}}')}{2(1 - \cos\Delta)} \left[\int_0^\Delta d\vartheta \, \sin\vartheta P_\ell(\cos\vartheta) + \int_{\pi-\Delta}^\pi d\vartheta \, \sin\vartheta P_\ell(\cos\vartheta) \right]. \tag{116}$$

Applying a change of coordinates with $u = \cos\vartheta$ yields

$$F^m_{\ell(\mathrm{cone})}(\hat{\mathbf{s}}', \Delta) = \frac{Y^{m*}_\ell(\hat{\mathbf{s}}')}{2(1 - \cos\Delta)} \left[\int_{\cos\Delta}^1 d\vartheta \, P_\ell(u) + \int_{-1}^{-\cos\Delta} d\vartheta \, P_\ell(u) \right]. \tag{117}$$

The Legendre polynomials $P_\ell(u)$ are even (odd) on the interval [-1, 1] when ℓ is even (odd), so the pair of integrals will be identical when ℓ is even and cancel when ℓ is odd. For even ℓ,

$$F^m_{\ell(\mathrm{cone})}(\hat{\mathbf{s}}', \Delta) = \frac{Y^{m*}_\ell(\hat{\mathbf{s}}')}{1 - \cos\Delta} \int_{\cos\Delta}^1 d\vartheta \, P_\ell(u). \tag{118}$$

The integral evaluates to [44, ch. 7.111]

$$\int_{\cos \Delta}^{1} d\vartheta \, P_{\ell}(u) = \begin{cases} 1 - \cos \Delta, & \ell = 0, \\ \sin \Delta \, P_l^{-1}(\cos \Delta), & \text{else,} \end{cases} \tag{119}$$

where $P_l^{-1}(\cos \Delta)$ is the associated Legendre polynomial with order $m = -1$, not an inverse Legendre polynomial. Bringing everything together

$$F_{\ell(\text{cone})}^m(\hat{\mathbf{s}}', \Delta) = \begin{cases} \sqrt{1/(4\pi)}, & \ell = 0, \\ 0, & \ell \text{ odd,} \\ Y_{\ell}^{m*}(\hat{\mathbf{s}}') \cot\left(\frac{\Delta}{2}\right) P_l^{-1}(\cos \Delta), & \ell > 0 \text{ even.} \end{cases} \tag{120}$$